

VIP Gas Separation Very Important Paper

How to cite: *Angew. Chem. Int. Ed.* **2020**, *59*, 17664–17669

International Edition: doi.org/10.1002/anie.202007681

German Edition: doi.org/10.1002/ange.202007681

Rational Design of Microporous MOFs with Anionic Boron Cluster Functionality and Cooperative Dihydrogen Binding Sites for Highly Selective Capture of Acetylene

Yuanbin Zhang, Jianbo Hu, Rajamani Krishna, Lingyao Wang, Lifeng Yang, Xili Cui, Simon Duttwyler,* and Huabin Xing*

Abstract: Separation of acetylene (C_2H_2) from carbon dioxide (CO_2) or ethylene (C_2H_4) is important in industry but limited by the low capacity and selectivity owing to their similar molecular sizes and physical properties. Herein, we report two novel dodecaborate-hybrid metal–organic frameworks, $MB_{12}H_{12}(dpb)_2$ (termed as BSF-3 and BSF-3-Co for $M = Cu$ and Co), for highly selective capture of C_2H_2 . The high C_2H_2 capacity and remarkable C_2H_2/CO_2 selectivity resulted from the unique anionic boron cluster functionality as well as the suitable pore size with cooperative proton-hydride dihydrogen bonding sites ($B-H^{\delta-} \cdots H^{\delta+}-C \equiv C-H^{\delta+} \cdots H^{\delta-}-B$). This new type of C_2H_2 -specific functional sites represents a fresh paradigm distinct from those in previous leading materials based on open metal sites, strong electrostatics, or hydrogen bonding.

Introduction

Acetylene (C_2H_2) is a critical fundamental raw material for the manufacture of various organic chemicals and polymers.^[1] It is generally produced from the cracking of hydrocarbons or partial combustion of natural gas, in which carbon dioxide (CO_2) inevitably coexists as a contaminant and needs to be removed to produce C_2H_2 in high purity.^[2] On the other hand, the deep removal of acetylene in the process of ethylene purification is greatly important since a trace amount of C_2H_2 can poison the catalysts for ethylene polymerization by forming metal acetylides.^[3] Current technologies for the separation and purification of C_2H_2 from other gases mainly rely on cryogenic distillation, partial

hydrogenation to ethylene by expensive metal catalysts, or solvent extraction, which are either cost-/energy-intensive or associated with pollution.^[4] On the other hand, physisorptive separation using porous materials has been demonstrated to be feasible to separate C_2H_2 from other gases in an efficient and eco-friendly manner. In this context, the development of acetylene-selective adsorbent materials is highly desirable.^[5] However, traditional porous materials such as zeolites, silica or activated carbons are challenged to separate C_2H_2/CO_2 (Figure 1 a,b) and C_2H_2/C_2H_4 (Supporting Information, Table S2) efficiently owing to the similar physicochemical properties of the gas molecules.

Metal–organic frameworks (MOFs),^[6] or porous coordination polymers (PCPs),^[7] have emerged as a new class of promising adsorbents for gas separation owing to their superior features such as tunable pore size and pore chemistry. These advanced characteristics have allowed the prospective design of target porous materials with desirable properties for specific gas separations.^[8] In this regard, several microporous MOFs that can selectively take up C_2H_2 from CO_2 or C_2H_4 have been reported.^[9] However, those exhibiting a high C_2H_2 capacity and high selectivity over both CO_2 and C_2H_4 are very rare. Two leading materials for both C_2H_2/CO_2 and C_2H_2/C_2H_4 separation are UTSA-300a^[2a] and TIFSIX-2-Cu-i.^[9b] UTSA-300a is a flexible MOF that can sieve C_2H_2 from CO_2 and C_2H_4 . However, the uptake of C_2H_2 on UTSA-300a under 1 bar and 298 K is modest (3.0 mmol g^{-1}) and the gate opening pressure for C_2H_2 is above 0.2 bar, which makes it difficult in practical conditions for efficient capture of C_2H_2

[*] Dr. Y. Zhang, Dr. J. Hu, L. Yang, Dr. X. Cui, Dr. H. Xing
Key Laboratory of Biomass Chemical Engineering of Ministry of Education, College of Chemical and Biological Engineering
Zhejiang University, Hangzhou 310027 (China)
and

Institute of Zhejiang University—Quzhou
78 Jiu Hua Boulevard North, Quzhou 324000 (P. R. China)
E-mail: xinghb@zju.edu.cn

Dr. L. Wang, Dr. S. Duttwyler
Department of Chemistry, Zhejiang University
310027 Hangzhou (P. R. China)
E-mail: duttwyler@zju.edu.cn

Dr. R. Krishna
Van't Hoff Institute for Molecular Sciences, University of Amsterdam
Science Park 904, 1098 XH Amsterdam (The Netherlands)

Supporting information and the ORCID identification number(s) for the author(s) of this article can be found under:
https://doi.org/10.1002/anie.202007681.

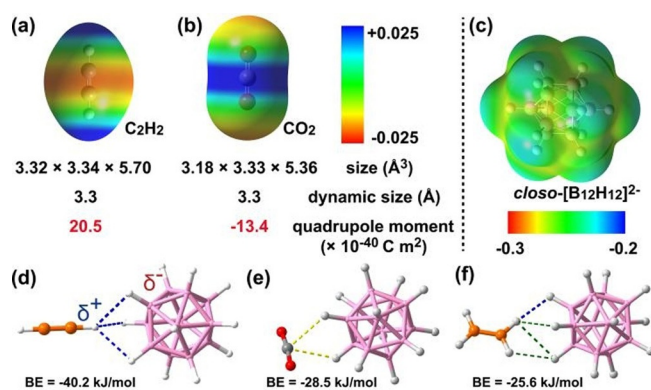


Figure 1. a)–c) Structure and electrostatic potentials of C_2H_2 (a), CO_2 (b) and $[B_{12}H_{12}]^{2-}$ (c). d)–f) DFT calculated bonding energy of single $closo-[B_{12}H_{12}]^{2-}$ anion with C_2H_2 (d), CO_2 (e), and C_2H_4 (f).

under low acetylene partial pressure. TIFSIX-2-Cu-i as a fluorinated anion (TiF_6^{2-})-hybrid MOF takes up a large amount of C_2H_2 (4.1 mmol g^{-1}) under 1 bar and 298 K. However, the IAST selectivity for $\text{C}_2\text{H}_2/\text{CO}_2$ is merely 6.5 since the uptake of CO_2 is even higher (4.3 mmol g^{-1}) under the same conditions owing to the strong $\text{Ti}-\text{F}^{\delta-}\cdots\text{C}^{\delta+}=\text{O}$ electrostatic interaction. Other functional sites including OMSs (open metal sites) and strong Lewis acidic/basic sites also usually possess similar affinity towards C_2H_2 and CO_2 , resulting in poor separation selectivity.^[8]

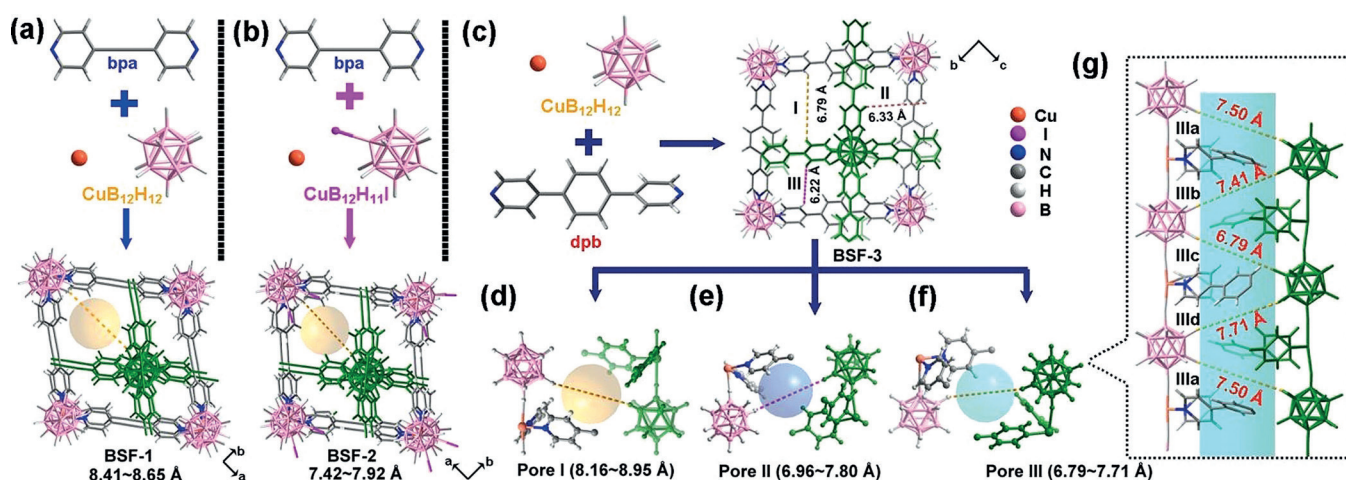
Results and Discussion

To boost the interaction with C_2H_2 but reduce the affinity towards CO_2 and C_2H_4 , we turned our attention to the anionic boron cluster functionality. Icosahedral *closo*-dodecaborate $[\text{B}_{12}\text{H}_{12}]^{2-}$ and its derivative $[\text{B}_{12}\text{H}_{11}\text{I}]^{2-}$ are highly stable symmetrical cluster boron anions that feature delocalized negative charges around the entire cage surface (Figure 1c).^[10] The $\text{B}-\text{H}^{\delta-}$ around the sphere surface can interact with C_2H_2 strongly through multiple proton-hydride dihydrogen bonds^[11] with the bonding energy (BE) up to $-40.2 \text{ kJ mol}^{-1}$ (Figure 1d) while the interaction with CO_2 (BE = $-28.5 \text{ kJ mol}^{-1}$) or C_2H_4 (BE = $-25.6 \text{ kJ mol}^{-1}$) is weaker, indicated by the density functional theory (DFT) calculation. Considering the inverse electrostatic potentials and quadrupole moment between C_2H_2 and CO_2 , we speculated that a porous material with two dodecaborate anions aligned in a reasonable distance will trap acetylene cooperatively inside by interacting with both terminal hydrogens and afford both high C_2H_2 binding affinity and capture capacity. With this in mind, we herein realized two novel analogous microporous metal-organic supramolecular frameworks termed as BSF-3 and BSF-3-Co by fine tuning the pore size and pore chemistry. They possess Cu or Co as nodes coordinated with 1,4-di(pyridin-4-yl)benzene (dpb) as organic linkers and *closo*-dodecaborate anions aligned inside the channels. The structure of BSF-3 was confirmed by single

crystal diffraction analysis while that of BSF-3-Co was postulated as an isostructural form. Gas adsorption studies revealed that both BSF-3 and BSF-3-Co show highly acetylene-selective adsorption with high capacity and selectivity over both CO_2 and C_2H_4 . The effective separation of these gases was further demonstrated by column-breakthrough experiments employing binary mixtures of $\text{C}_2\text{H}_2/\text{CO}_2$ and $\text{C}_2\text{H}_2/\text{C}_2\text{H}_4$ with good recyclability. Modelling studies indicated the high acetylene capacity and excellent selectivity of $\text{C}_2\text{H}_2/\text{CO}_2$ were attributed to the anionic boron cluster functionality as well as the suitable pore size with desirable cooperative dihydrogen bonding ($\text{B}-\text{H}^{\delta-}\cdots\text{H}^{\delta+}-\text{C}\equiv\text{C}-\text{H}^{\delta+}\cdots\text{H}^{\delta-}-\text{B}$) sites. Notably, this C_2H_2 -specific functional sites not only enhance the affinity of the BSFs towards C_2H_2 but also reduce the interactions with CO_2 and C_2H_4 , which represents a fresh paradigm shift from those in previous top materials based on open metal sites, strong hydrogen bonding or electrostatics.

The adsorption experiments were initially conducted on our two recently developed materials BSF-1 and BSF-2.^[12,13] BSF-1 was self-assembled from $\text{Cu}[\text{B}_{12}\text{H}_{12}]$ and 1,2-bis(4-pyridyl)acetylene (bpa) with the opposite $\text{H}(\text{B})\cdots\text{H}(\text{B})$ distance at 8.41–8.65 Å, while BSF-2 was constructed by $[\text{B}_{12}\text{H}_{11}\text{I}]^{2-}$, Cu^{2+} and bpa (Scheme 1a,b). The porous structures were similar between BSF-1 and BSF-2 with only the largest pores available for guest molecules while BSF-2 exhibited contract pore size with $\text{H}(\text{B})\cdots\text{H}(\text{B})$ length of 7.92 Å and $\text{H}(\text{B})\cdots\text{I}(\text{B})$ length of 7.42 Å. The C_2H_2 , C_2H_4 and CO_2 uptakes at 298 K and 1 bar were 2.35/1.63/1.77 mmol g^{-1} for BSF-1 and 1.85/1.32/1.33 mmol g^{-1} for BSF-2 (Supporting Information, Figures S12, S13). The equimolar IAST selectivity calculated for $\text{C}_2\text{H}_2/\text{CO}_2$ and $\text{C}_2\text{H}_2/\text{C}_2\text{H}_4$ were 3.4:2.4 for BSF-1 and 5.1:2.9 for BSF-2. Such modest acetylene capacity and selectivity may result from the fact that only the largest pore is accessible while the other 3 pores are ineffective for uptake as well as the overlong $\text{H}(\text{B})\cdots\text{H}(\text{B})$ distances that fail to trap C_2H_2 tightly inside.

Based on the initial findings, we hypothesized that 1,4-di(pyridin-4-yl)benzene (dpb, 11.4 Å for opposite N-N dis-



Scheme 1. Fine-tuning the pore size in BSF-*n* (*n* = 1, 2, 3) materials by choosing different dodecaborate pillars and dipyrindyl ligands. All displayed structures are based on X-ray crystallography.^[19]

tance) would serve as an optimized organic linker instead of bpa (9.6 Å) in BSF-1 and BSF-2. A novel microporous metal organic supramolecular framework termed as BSF-3 was successfully prepared by the reaction of $\text{Na}_2[\text{B}_{12}\text{H}_{12}]$, $\text{Cu}(\text{NO}_3)_2 \cdot 3\text{H}_2\text{O}$, and dpb in $\text{MeOH}/\text{H}_2\text{O}$ solution at 75 °C for 48 h (Scheme 1 c). Single crystals of BSF-3 were prepared by slow diffusion of aqueous $\text{Na}_2[\text{B}_{12}\text{H}_{12}]/\text{CuNO}_3 \cdot 3\text{H}_2\text{O}$ into a MeOH solution of dpb. X-ray structural analysis of BSF-3 reveals that it crystallizes in a three-dimensional framework in the orthorhombic space group $\text{Ima}2$ (Supporting Information, Table S1). The rhombohedral cavities defined by $\text{Cu}\cdots\text{Cu}$ distances are of the dimension of $15.3 \times 15.3 \times 9.9 \text{ \AA}^3$, in which the $\text{Cu}\cdots\text{Cu}$ linked by dipyrindyl linkers were much elongated compared to the $\text{Cu}\cdots\text{Cu}$ distance of 13.6 Å for BSF-1 and BSF-2. A two-fold offset interpenetration is observed, which leads to four crystallographically distinct channels with void space of 28.1 % calculated by PLATON with a probe radius of 1.2 Å (Supporting Information, Figures S2). Owing to the extension of dipyrindyl linkers, there are 3 pores (pore window size: 6.79, 6.22 and 6.33 Å defined by the $\text{H}(\text{C})\cdots\text{H}(\text{C})$ distance) large enough to accommodate guest molecules. Pore II and Pore III are similar in shape, but different in the pore chemistry owing to the distinct rotational geometry of aromatic rings (Scheme 1 d–f).

First of all, single component N_2 adsorption at 77 K was measured (Supporting Information, Figure S14), which indicated that BSF-3 has a BET surface area of $458 \text{ m}^2 \text{ g}^{-1}$. Interestingly when we used $\text{Co}(\text{NO}_3)_2 \cdot 6\text{H}_2\text{O}$ in place of $\text{Cu}(\text{NO}_3)_2 \cdot 3\text{H}_2\text{O}$, a novel isostructural supramolecular framework was generated, named as BSF-3-Co. 77 K N_2 adsorption indicated that BSF-3-Co has a BET surface area of $437 \text{ m}^2 \text{ g}^{-1}$ (Supporting Information, Figure S15), similar to those of BSF-3. Moreover, the pore size distribution calculated from the N_2 adsorption was highly close for BSF-3 and BSF-3-Co, indicating the analogous porous characteristics (Supporting

Information, Figure S16). The similarity of BSF-3 and BSF-3-Co were further confirmed by IR spectroscopy (Supporting Information, Figures S7, S8), TGA analysis (Figure S9) and EPR spectroscopy (Supporting Information, Figures S10).

The establishment of permanent microporosity in BSF-3 and BSF-3-Co motivated us to study the gas separation performance for $\text{C}_2\text{H}_2/\text{CO}_2$ and $\text{C}_2\text{H}_2/\text{C}_2\text{H}_4$. At first, single component C_2H_2 , CO_2 and C_2H_4 adsorption measurements at 298 K were conducted. At 1.0 bar, the $\text{C}_2\text{H}_2/\text{CO}_2/\text{C}_2\text{H}_4$ uptakes were 3.59/2.11/2.37 mmol g^{-1} for BSF-3 and 3.85/2.41/2.51 mmol g^{-1} for BSF-3-Co, respectively (Figure 2 a–c). Notably, the C_2H_2 uptake on BSF-3-Co was nearly two-fold compared to that on BSF-1 and BSF-2 (Figure 2a). The selectivity for equimolar $\text{C}_2\text{H}_2/\text{CO}_2$ and $\text{C}_2\text{H}_2/\text{C}_2\text{H}_4$ gas mixtures on BSFs at 298 K were calculated using ideal adsorbed solution theory (IAST) after fitting isotherms to the Langmuir-Freundlich equation until excellent accuracy (for details, see the Supporting Information). Figure 2 d,e reveal that the selectivity for equimolar $\text{C}_2\text{H}_2/\text{CO}_2$ and $\text{C}_2\text{H}_2/\text{C}_2\text{H}_4$ at 298 K and 1.0 bar are 16.3 and 8.0 for BSF-3, 12.7 and 10.2 for BSF-3-Co, respectively. This $\text{C}_2\text{H}_2/\text{CO}_2$ selectivity on BSF-3 is higher than that of many leading materials such as MUF-17 (6.0),^[9a] TIFSIX-2-Ni-i (6.1),^[9d] TIFSIX-2-Cu-i (6.5),^[9b] UTSA-74 (9),^[14] JCM-1 (13.7),^[9c] DICRO-4-Ni-i (13.9)^[9e] under the same conditions (Figure 1 g). The $\text{C}_2\text{H}_2/\text{CO}_2$ (2:1) selectivity at 0.15 bar (which represents the combined proportion of CO_2 and C_2H_2 concentrations in relevant industrial gas streams) is 15.6 for BSF-3 and 15.0 for BSF-3-Co. Other well-performing porous materials such as HOF-3a,^[15] $\text{Ni}(\text{HCOO})_6$ ^[16] and NKMOF-1-Ni^[17] exhibit higher $\text{C}_2\text{H}_2/\text{CO}_2$ selectivity but much lower capacity for C_2H_2 (Figure 1 g). A comprehensive comparison of porous materials in the context of $\text{C}_2\text{H}_2/\text{CO}_2$ and $\text{C}_2\text{H}_2/\text{C}_2\text{H}_4$ separation was listed in the Supporting Information, Table S13, in which BSF-3 and BSF-3-Co still rank the top.

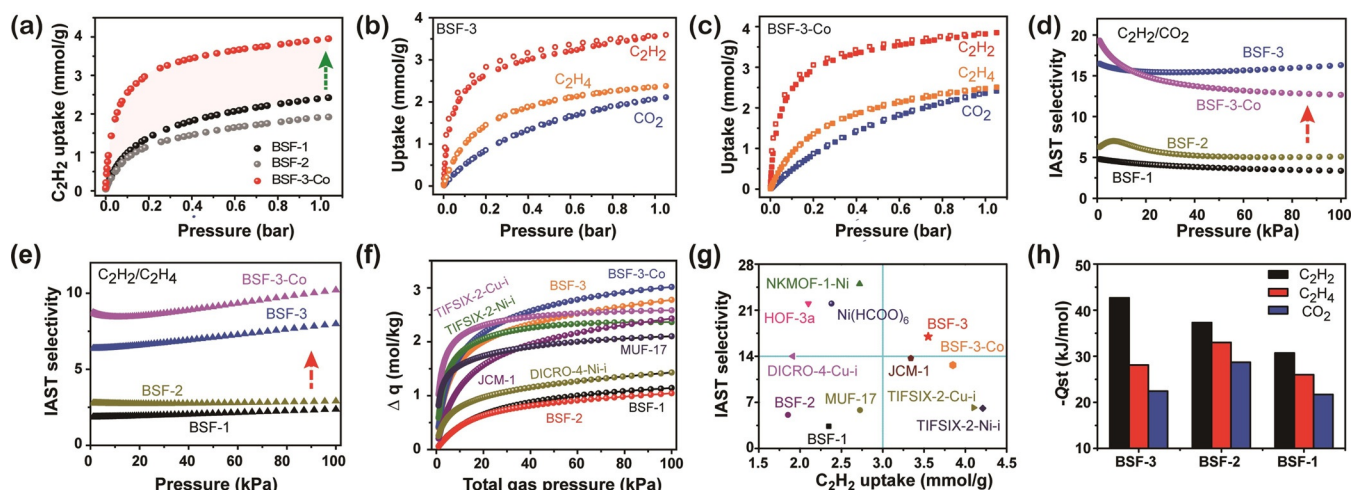


Figure 2. a) C_2H_2 adsorption isotherms for BSF-3, BSF-2, and BSF-1 at 298 K. b) C_2H_2 , C_2H_4 , and CO_2 adsorption and desorption isotherms for BSF-3 at 298 K. c) C_2H_2 , C_2H_4 , and CO_2 adsorption and desorption isotherms for BSF-3-Co at 298 K. d) IAST adsorption selectivity of BSFs toward a 1:1 mixture of $\text{C}_2\text{H}_2/\text{CO}_2$. e) IAST adsorption selectivity of BSFs toward a 1:1 mixture of $\text{C}_2\text{H}_2/\text{C}_2\text{H}_4$. f) Comparison of the capacity difference of the BSF materials ($\Delta q = \text{C}_2\text{H}_2$ uptake – CO_2 uptake) to uptake C_2H_2 and CO_2 from $\text{C}_2\text{H}_2/\text{CO}_2$ (50:50) mixtures with reported well-performing materials based on IAST calculation. g) Comparison of the IAST selectivity of $\text{C}_2\text{H}_2/\text{CO}_2$ and C_2H_2 adsorption capacity at 298 K and 1 bar among reported well-performing materials. h) Comparison of the Q_{st} for C_2H_2 , C_2H_4 and CO_2 adsorption on BSF-3, BSF-2 and BSF-1.

The static C_2H_2 and CO_2 uptake from the equimolar mixture of C_2H_2/CO_2 were calculated for BSFs and other leading materials. The capacity differences (Δq) between C_2H_2 and CO_2 uptake were compared, which showed a trend of $BSF-3-Co$ (3.01 mmol g^{-1}) > $BSF-3$ (2.78 mmol g^{-1}) > $TIFSIX-2-Cu-i$ (2.58 mmol g^{-1}) > $JCM-1$ (2.43 mmol g^{-1}) > $TIFSIX-2-Ni-i$ (2.36 mmol g^{-1}) > $MUF-17$ (2.10 mol g^{-1}) > $DICRO-4-Ni-i$ (1.43 mmol g^{-1}) > $BSF-1$ (1.14 mmol g^{-1}) > $BSF-2$ (1.04 mmol g^{-1}) at 100 kPa and 298 K (Figure 1 f). The C_2H_2 , C_2H_4 and CO_2 adsorption isotherms were further collected at 273 K and 313 K and all revealed type I isotherms (Supporting Information, Figures S17–S22). The isosteric enthalpy of adsorption (Q_{st}) for $BSF-1$, $BSF-2$, and $BSF-3$ was further calculated using the Clausius–Clapeyron equation for comparison. Q_{st} values at near-zero loading for C_2H_2 , CO_2 , and C_2H_4 were -42.7 , -22.4 , and $-28.1 \text{ kJ mol}^{-1}$ for $BSF-3$ (Figure 2 h). Such distinct Q_{st} values also give evidence for the preferential adsorption of C_2H_2 over CO_2 and C_2H_4 . Additionally, the absolute Q_{st} value for C_2H_2 in $BSF-3$ is much higher than those in $BSF-2$ ($-37.3 \text{ kJ mol}^{-1}$) and $BSF-1$ ($-30.7 \text{ kJ mol}^{-1}$) as well as many other C_2H_2 physisorbent materials including $JCM-1$ ($-36.9 \text{ kJ mol}^{-1}$),^[9c] $DICRO-4-Ni-i$ ($-37.7 \text{ kJ mol}^{-1}$),^[18b] $UTSA-74$ (-32 kJ mol^{-1})^[13] and so on. However, the absolute Q_{st} value for CO_2 in $BSF-3$ is similar to that in $BSF-1$ ($-21.7 \text{ kJ mol}^{-1}$), and much lower than those in $BSF-2$ ($-28.7 \text{ kJ mol}^{-1}$), $JCM-1$ ($-33.4 \text{ kJ mol}^{-1}$) and $DICRO-4-Ni-i$ ($-33.9 \text{ kJ mol}^{-1}$). These results indicated an enhanced affinity difference towards C_2H_2 and CO_2 , consistent with the excellent C_2H_2/CO_2 selectivity on $BSF-3$.

To gain insight into the gas adsorption behavior, modeling studies using grand canonical Monte Carlo (GCMC) simulations were performed. The results showed that acetylene is able to enter Pores I–III both at low and high pressure (1 and 100 kPa). The number of C_2H_2 molecules located in pores follows the order of Pore III > Pore II \approx Pore I (Supporting Information, Figures S43–S46). Distinct $B-H^{\delta-} \cdots H^{\delta+}-C$ dihydrogen bonds can be observed (Figure 3 a). The simulated $-Q_{st}$ was 34 kJ mol^{-1} under low coverage loading, slightly lower than the experimental value due to the underestimation of the strong cooperative dihydrogen interactions between C_2H_2 and $[B_{12}H_{12}]^{2-}$ in the framework. DFT calculations were

further utilized to more accurately analyze the bonding position and binding energy of C_2H_2 , C_2H_4 and CO_2 by isolating the effective $[B_{12}H_{12}]^{2-}$ clusters in the surface of Pore IIIb, which indicated that C_2H_2 was tightly trapped by two opposite dodecaborates through cooperative $B-H^{\delta-} \cdots H^{\delta+}-C \equiv C-H^{\delta+} \cdots H^{\delta-}-B$ dihydrogen bonds (2.35 and 2.38 Å) with a bonding energy of $-41.8 \text{ kJ mol}^{-1}$ (Figure 3 b), very close to the experimental Q_{st} value. This cooperative 1 + 1 dihydrogen bonding is even stronger than 3 dihydrogen bonds between single dodecaborate and C_2H_2 (Figure 3 b vs. Figure 1 d). However, this enhanced interaction is not observed in CO_2 or C_2H_4 adsorption. In sharp contrast, the interaction between two dodecaborates and CO_2 or C_2H_4 is even weaker than that between single dodecaborate and CO_2 (Figure 3 c, from -28.5 to $-25.5 \text{ kJ mol}^{-1}$) or C_2H_4 (Supporting Information, Figure S41b, from -26.5 to $-21.5 \text{ kJ mol}^{-1}$). For $BSF-1$, GCMC simulations indicated that C_2H_2 is only adsorbed in the largest pore (Supporting Information, Figure S47). Therefore, the enhanced capacity and selectivity can be explained by: 1) creation of more accessible pores for improved accommodation room; and 2) construction of cooperative dihydrogen bonding sites from unique boron cluster functionality as C_2H_2 -specific sweet spot. Further DFT calculation predicted that the $H(B) \cdots H(B)$ distances in 6.7–7.7 Å or the distances of two dodecaborate centers in 10–13 Å are favorable for forming cooperative dihydrogen bonding with C_2H_2 (Supporting Information, Tables S11, S12). This can be used as an important clue to design boron cluster based porous materials for efficient acetylene capture in the future.

Transient breakthrough simulations were conducted for C_2H_2/CO_2 (50:50) and C_2H_2/C_2H_4 (1:99) mixtures to demonstrate the gas separation performance of BSF materials in column adsorption process.^[18] As we failed to know the crystal density data of guest-free $BSF-3-Co$, the simulations were performed only for $BSF-1$, $BSF-2$, and $BSF-3$. Clean separations were achieved (Figures 4 a,b). Other representative materials for C_2H_2/CO_2 separation such as $DICRO-4-Ni-i$, $JCM-1$, $TIFSIX-2-Cu-i$, $TIFSIX-2-Ni-i$, and $MUF-17$ were also calculated for comparison, among which $BSF-3$ exhibits the highest Δq_{break} (2.44 mol kg^{-1}) values, indicating the best separation ability for C_2H_2/CO_2 separation (Supporting Information, Figure S32, Table S10). Moreover, a linear correlation ($R^2 = 0.995$) between Δq_{IAST} based on static IAST calculation and Δq_{break} based on transient breakthrough simulations was observed, while all the Δq_{break} values were slightly lower than the corresponding Δq_{IAST} values due to the distended nature of the breakthroughs in the fixed bed (Figure 4 c). Based on the linear relationship, the Δq_{break} for $BSF-3-Co$ was supposed to be as high as about 2.7 mol kg^{-1} .

To evaluate the practical gas separation performance, dynamic breakthrough experiments with several different ratios of C_2H_2/CO_2 and C_2H_2/C_2H_4 mixtures were conducted on $BSF-1$ and $BSF-3$ for comparison. First of all, breakthrough experiments with equimolar C_2H_2/CO_2 mixture (Figure 4 d) are conducted for $BSF-3$ at 298 K and 1.0 bar. CO_2 was eluted first while C_2H_2 retained in the column for longer time. The calculated acetylene captured in the column was about 2.9 mmol g^{-1} , which is highly consistent with the simulated acetylene capacity of 2.96 mmol g^{-1} . To simulate

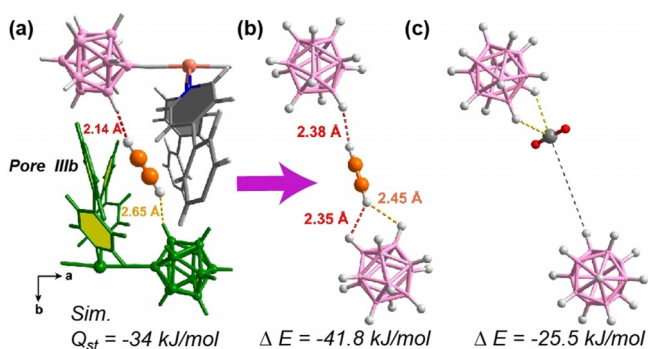


Figure 3. a) A snapshot from GCMC simulation results for C_2H_2 adsorption in pore IIIb of $BSF-3$. b) DFT calculation optimized C_2H_2 adsorption configuration in pore IIIb. The carbon atoms of C_2H_2 were highlighted in orange. c) DFT calculation optimized CO_2 adsorption configuration in pore IIIb.

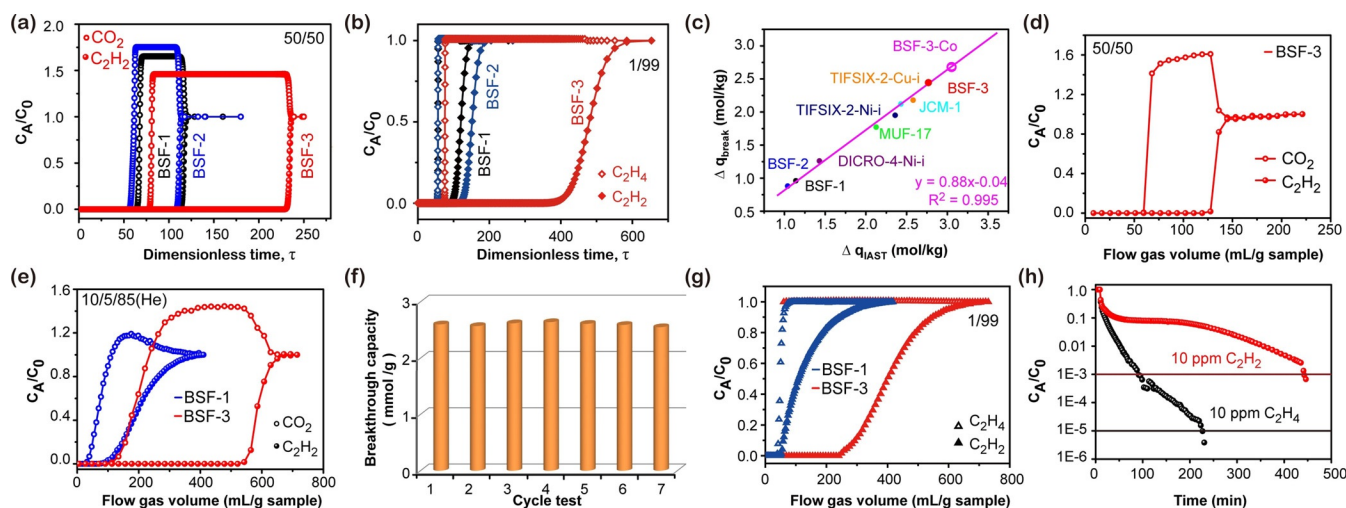


Figure 4. a) simulated breakthrough curves of BSFs for C_2H_2/CO_2 (50:50) separation. b) Simulated breakthrough curves of BSFs for C_2H_2/C_2H_4 (1:99) separation. c) Plots of the calculated separation potential Δq_{break} in the fixed bed with the calculated separation potential Δq_{IAST} from the static adsorption isotherms for equimolar C_2H_2/CO_2 mixture. d) The experimental column breakthrough curves of BSF-3 for C_2H_2/CO_2 (50:50) separation. e) The experimental column breakthrough curves of BSF-3 (red) and BSF-1 (blue) for $C_2H_2/CO_2/He$ (10:5:85) separation. f) The cycling test of BSF-3 for $C_2H_2/CO_2/He$ (10:5:85) separation. g) The experimental column breakthrough curves of BSF-3 (red) and BSF-1 (blue) for C_2H_2/C_2H_4 (1:99) separation. h) Regeneration test of BSF-3 by purging a He flow (5 mL min^{-1}) at 25°C .

the practical relative proportions of C_2H_2 and CO_2 in gas streams for acetylene production, breakthrough experiments in which a gas mixture comprising $C_2H_2/CO_2/He$ (10:5:85%) were conducted for BSF-3 and BSF-1. Figure 2e shows the breakthrough curves of BSF-3 and BSF-1 for C_2H_2/CO_2 mixture. As shown, only CO_2 , which has a lower affinity, appeared at the outlet of the column at the initial stage. C_2H_2 breakthrough occurred after about 76 min for BSF-3 (Supporting Information, Figure S35). Furthermore, the stability of BSF-3 under multiple adsorption-desorption cycles was evaluated by cycling breakthrough experiments. BSF-3 showed decent regenerability at a mild desorption condition (N_2 purge for 8 h at 50°C with a flow of 5 mL min^{-1}) with consistent C_2H_2 capacity over 7 cycles (Figures 4f). The breakthrough experiments with a C_2H_2/C_2H_4 (1:99) mixture indicated that BSF-3 had a good ability for deep removal of trace acetylene while BSF-1 performed less efficiently (Figure 4g). After BSF-3 was saturated by the C_2H_2/C_2H_4 gas mixture, the column was purged with a He flow (5 mL min^{-1}) at 25°C and outlet gas concentration was monitored. The results showed that the outlet concentration of C_2H_4 reduced to 10 ppm after about 4 h while the outlet concentration of C_2H_2 dropped to 10 ppm after about 7 h, which further indicated the easy regeneration of BSF-3 (Figure 4h).

Conclusion

Two isostructural boron cluster-functionalized microporous supramolecular metal-organic frameworks BSF-3 and BSF-3-Co were rationally designed for the efficient separation of C_2H_2/CO_2 and C_2H_2/C_2H_4 . The excellent separation performances are fully studied by static adsorption isotherms, dynamic breakthrough experiments, and modeling studies. Notable features include: 1) excellent C_2H_2/CO_2 and $C_2H_2/$

C_2H_4 separation selectivity; 2) high C_2H_2 capacity under ambient conditions; 3) good recyclability for dynamic separation. The high acetylene capacity and remarkable selectivity of C_2H_2/CO_2 were attributed to the anionic boron cluster functionality as well as the suitable pore size with cooperative dihydrogen bonding sites ($B-H^{\delta-}\cdots H^{\delta+}-C\equiv C-H^{\delta+}\cdots H^{\delta-}-B$), revealed by modeling studies. This C_2H_2 -specific functional sites not only enhance the affinity of the MOFs towards C_2H_2 but also reduce the interactions with CO_2 and C_2H_4 , representing a fresh paradigm shift from those in previous top materials based on open metal sites, strong hydrogen bonding or electrostatics. In general, our work demonstrates the importance of the boron cluster functionality as well as the fine-tuning of pore size/shape to form cooperative interactions in porous materials for gas separation.

Acknowledgements

This work was supported by the Natural Science Foundation of China (No. 21908193, 21938011, 21725603), the China Postdoctoral Science Foundation (NO. 2018M642434) and National Program for Support of Top-notch Young Professionals (H.X.).

Conflict of interest

The authors declare no conflict of interest.

Keywords: adsorption · cooperative interaction · dodecaborate · gas separation · metal-organic frameworks

- [1] P. J. Stang, F. Diederich, *Modern Acetylene Chemistry*, Wiley-VCH, Weinheim, **2008**.
- [2] a) R.-B. Lin, L. Li, H. Wu, H. Arman, B. Li, R.-G. Lin, W. Zhou, B. Chen, *J. Am. Chem. Soc.* **2017**, *139*, 8022–8028; b) C. Zhang, L. Wang, G. Maurin, Q. Yang, *AIChE J.* **2018**, *64*, 4089–4096; c) L. Zhang, K. Jiang, L. Li, Y.-P. Xia, T.-L. Hu, Y. Yang, Y. Cui, B. Li, B. Chen, G. Qian, *Chem. Commun.* **2018**, *54*, 4846–4849.
- [3] a) J. Li, L. Jiang, S. Chen, A. Krichon, B. Li, Y. Li, H. C. Zhou, *J. Am. Chem. Soc.* **2019**, *141*, 3807–3811; b) X. Cui, K. Chen, H. Xing, Q. Yang, R. Krishna, Z. Bao, H. Wu, W. Zhou, X. Dong, Y. Han, B. Li, Q. Ren, M. J. Zaworotko, B. Chen, *Science* **2016**, *353*, 141–144.
- [4] D. S. Sholl, R. P. Lively, *Nature* **2016**, *532*, 435–438.
- [5] a) B. R. Barnett, M. I. Gonzalez, J. R. Long, *Trends Chem.* **2019**, *1*, 159–171; b) K. Adil, Y. Belmabkhout, R. S. Pillai, A. Cadiau, P. M. Bhatt, A. H. Assen, G. Maurin, M. Eddaoudi, *Chem. Soc. Rev.* **2017**, *46*, 3402–3430; c) X. Zhao, Y. Wang, D. S. Li, X. Bu, P. Feng, *Adv. Mater.* **2018**, *30*, 1705189.
- [6] a) M. Ding, R. W. Flaig, H.-L. Jiang, O. M. Yaghi, *Chem. Soc. Rev.* **2019**, *48*, 2783–2828; b) B. Li, M. Chrzanowski, Y. Zhang, S. Ma, *Coord. Chem. Rev.* **2016**, *307*, 106–129; c) L. Yang, S. Qian, X. Wang, X. Cui, B. Chen, H. Xing, *Chem. Soc. Rev.* **2020**, <https://doi.org/10.1039/c9cs00756c>.
- [7] a) N. Hosono, A. Terashima, S. Kusaka, R. Matsuda, S. Kitagawa, *Nat. Chem.* **2019**, *11*, 109–116; b) M. Inukai, M. Tamura, S. Horike, M. Higuchi, S. Kitagawa, K. Nakamura, *Angew. Chem. Int. Ed.* **2018**, *57*, 8687–8690; *Angew. Chem.* **2018**, *130*, 8823–8826; c) I. E. Claassens, V. I. Nikolayenko, D. A. Haynes, L. J. Barbour, *Angew. Chem. Int. Ed.* **2018**, *57*, 15563–15566; *Angew. Chem.* **2018**, *130*, 15789–15792.
- [8] a) H. Wang, J. Li, *Acc. Chem. Res.* **2019**, *52*, 1968–1978; b) L. Yang, X. Cui, Z. Zhang, Q. Yang, Z. Bao, Q. Ren, H. Xing, *Angew. Chem. Int. Ed.* **2018**, *57*, 13145–13149; *Angew. Chem.* **2018**, *130*, 13329–13333; c) P.-Q. Liao, N.-Y. Huang, W.-X. Zhang, J.-P. Zhang, X.-M. Chen, *Science* **2017**, *356*, 1193–1196; d) R.-B. Lin, S. Xiang, W. Zhou, B. Chen, *Chem* **2020**, *6*, 337–363.
- [9] a) O. T. Qazvini, R. Babarao, S. G. Telfer, *Chem. Mater.* **2019**, *31*, 4919–4926; b) K. J. Chen, H. S. Scott, D. G. Madden, T. Pham, A. Kumar, A. Bajpai, M. Lusi, K. A. Forrest, B. Space, J. J. Perry IV, M. J. Zaworotko, *Chem* **2016**, *1*, 753–765; c) J. Lee, C. Y. Chuah, J. Kim, Y. Kim, N. Ko, Y. Seo, K. Kim, T. H. Bae, E. Lee, *Angew. Chem. Int. Ed.* **2018**, *57*, 7869–7873; *Angew. Chem.* **2018**, *130*, 7995–7999; d) M. Jiang, X. Cui, L. Yang, Q. Yang, Z. Zhang, Y. Yang, H. Xing, *Chem. Eng. J.* **2018**, *352*, 803–810;
- e) H. S. Scott, M. Shivanna, A. Bajpai, D. G. Madden, K.-J. Chen, T. Pham, K. A. Forrest, A. Hogan, B. Space, J. J. Perry IV, M. J. Zaworotko, *ACS Appl. Mater. Interfaces* **2017**, *9*, 33395–33400.
- [10] a) J. C. Axtell, L. M. Saleh, E. A. Qian, A. I. Wixtrom, A. M. Spokoiny, *Inorg. Chem.* **2018**, *57*, 2333–2350; b) R. Núñez, I. Romero, F. Teixidor, C. Viñas, *Chem. Soc. Rev.* **2016**, *45*, 5147–5173; c) Y. Zhang, Y. Sun, F. Lin, J. Liu, S. Duttwyler, *Angew. Chem. Int. Ed.* **2016**, *55*, 15609–15614; *Angew. Chem.* **2016**, *128*, 15838–15843.
- [11] a) V. I. Bakhmutov, *Dihydrogen Bonds: Principles, Experiments, and Applications*, Wiley, Hoboken, **2008**.
- [12] a) Y. Zhang, L. Yang, L. Wang, S. Duttwyler, H. Xing, *Angew. Chem. Int. Ed.* **2019**, *58*, 8145–8150; *Angew. Chem.* **2019**, *131*, 8229–8234; b) Y. Zhang, L. Yang, L. Wang, H. Xing, *J. Mater. Chem. A* **2019**, *7*, 27560–27566.
- [13] D. Jung, F. Raffan-Montoya, R. Ramachandran, Y. Zhang, T. Islamoglu, G. Marin, E. A. Qian, R. M. Dziedzic, O. K. Farha, S. I. Stoliarov, A. M. Spokoiny, *Chem. Commun.* **2019**, *55*, 8852–8855.
- [14] F. Luo, C. Yan, L. Dang, R. Krishna, W. Zhou, H. Wu, X. L. Dong, Y. Han, T.-L. Hu, M. O’Keeffe, L. Wang, M. Luo, R.-B. Lin, B. Chen, *J. Am. Chem. Soc.* **2016**, *138*, 5678–5684.
- [15] P. Li, Y. B. He, Y. F. Zhao, L. H. Weng, H. L. Wang, R. Krishna, H. Wu, W. Zhou, M. O’Keeffe, Y. Han, B. L. Chen, *Angew. Chem. Int. Ed.* **2015**, *54*, 574–577; *Angew. Chem.* **2015**, *127*, 584–587.
- [16] L. Zhang, K. Jiang, J. Zhang, J. Pei, K. Shao, Y. Cui, Y. Yang, B. Li, B. Chen, G. Qian, *ACS Sustainable Chem. Eng.* **2019**, *7*, 1667–1672.
- [17] Y.-L. Peng, T. Pham, P. Li, T. Wang, Y. Chen, K.-J. Chen, K. A. Forrest, B. Space, P. Cheng, M. J. Zaworotko, Z. Zhang, *Angew. Chem. Int. Ed.* **2018**, *57*, 10971–10975; *Angew. Chem.* **2018**, *130*, 11137–11141.
- [18] a) R. Krishna, *RSC Adv.* **2017**, *7*, 35724–35737; b) R. Krishna, *Sep. Purif. Technol.* **2018**, *194*, 281–300.
- [19] Deposition Number 1956266 (for BSF-3) contains the supplementary crystallographic data for this paper. These data are provided free of charge by the joint Cambridge Crystallographic Data Centre and Fachinformationszentrum Karlsruhe Access Structures service www.ccdc.cam.ac.uk/structures.

Manuscript received: May 28, 2020

Accepted manuscript online: June 26, 2020

Version of record online: August 6, 2020

Supporting Information

Rational Design of Microporous MOFs with Anionic Boron Cluster Functionality and Cooperative Dihydrogen Binding Sites for Highly Selective Capture of Acetylene

*Yuanbin Zhang, Jianbo Hu, Rajamani Krishna, Lingyao Wang, Lifeng Yang, Xili Cui,
Simon Duttwyler,* and Huabin Xing**

anie_202007681_sm_miscellaneous_information.pdf

Supporting Information

I	General information and procedures	p. S3–S11
II	Characterization (X-ray Crystallography IR, TGA and EPR)	p. S12–S18
III	Adsorption data, IAST selectivity and Q_{st}	p. S19–S30
IV	Breakthrough simulations	p. S31–S32
V	Breakthrough experiment data	p. S33–S37
VI	DFT calculations and GCMC simulations	p. S38–S43
VII	Stability test	p. S44-49
VIII	Adsorption selectivity comparison table	p. S50–51
	References	p. S52-54

I. General Information and Procedures

Chemicals: $\text{Cu}[\text{NO}_3]_2 \cdot 3\text{H}_2\text{O}$ and $\text{Co}[\text{NO}_3]_2 \cdot 6\text{H}_2\text{O}$ were purchased from Adamas-beta and used without further purification. 1,4-di(pyridin-4-yl)benzene and 1,2-bis(4-pyridyl)acetylene were ordered from Chemsoon and recrystallized before use. $[\text{Na}]_2[\text{B}_{12}\text{H}_{12}]$, $[\text{Na}]_2[\text{B}_{12}\text{H}_{11}\text{I}]$ were prepared based on reported methods and recrystallized from hot MeOH before use.^[1]

Preparation of BSF-1

Bulky synthesis: A mixture of $[\text{Na}]_2[\text{B}_{12}\text{H}_{12}]$ (225 mg, 1.2 mmol, 1.2 equiv) and $\text{Cu}[\text{NO}_3]_2 \cdot 3\text{H}_2\text{O}$ (242 mg, 1 mmol, 1 equiv) was dissolved in 10 mL of water in a 100 mL round bottom flask. Then a MeOH (15 mL) solution of 1, 2-bis(4-pyridyl)acetylene (360 mg, 2 mmol, 2 equiv) was slowly added to the above aqueous solution. A violet solid precipitated immediately, and the suspension was stirred at 25 °C for 24 h. The solid was collected by filtration, washed by MeOH, and re-soaked in MeOH for further use.

Preparation of BSF-2

A mixture of $[\text{Na}]_2[\text{B}_{12}\text{H}_{11}\text{I}]$ (314 mg, 1 mmol, 1 equiv) and $\text{Cu}[\text{NO}_3]_2 \cdot 3\text{H}_2\text{O}$ (242 mg, 1 mmol, 1 equiv) was dissolved in 10 mL of water in a 100 mL round bottom flask. Then a MeOH (15 mL) solution of 1, 2-bis(4-pyridyl)acetylene (360 mg, 2 mmol, 2 equiv) was slowly added to the above aqueous solution. A violet solid precipitated immediately, and the suspension was stirred at 25 °C for 24 h. The solid was collected by filtration, washed by MeOH, and re-soaked in MeOH for further use.

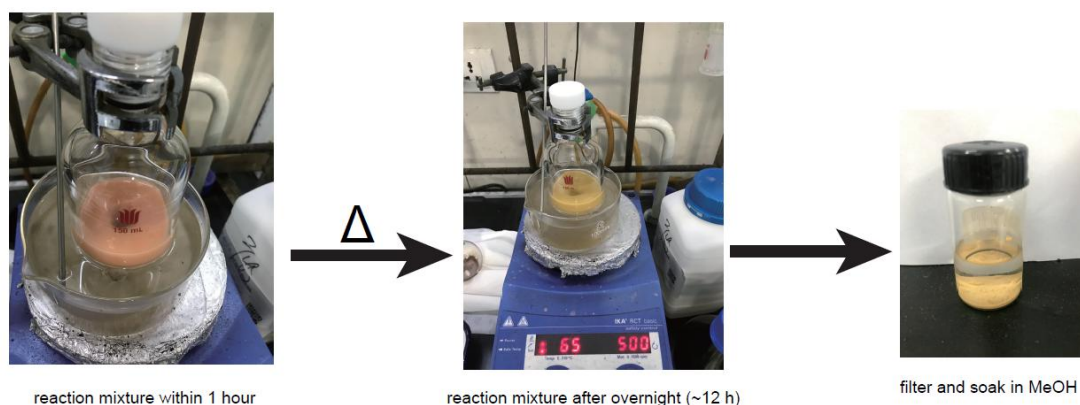
Preparation of BSF-3

Bulky synthesis: A mixture of $[\text{Na}]_2[\text{B}_{12}\text{H}_{12}]$ (225 mg, 1.2 mmol, 1.2 equiv) and $\text{Cu}[\text{NO}_3]_2 \cdot 3\text{H}_2\text{O}$ (242 mg, 1 mmol, 1 equiv) was dissolved in 10 mL of water in a 100 mL bottle and heated to 75 °C. Then a MeOH (30 mL) solution of 1,4-di(pyridin-4-yl)benzene (dpa) (464 mg, 2 mmol, 2 equiv) was slowly added to the above solution. The bottle was well sealed; gray violet solid formed immediately, and the suspension was stirred at 75 °C for another 48 h. The solid was then collected by filtration, washed by MeOH (10 mL), followed by: (a) soaked in anhydrous MeOH for further use (BSF-3 was stable in dry MeOH for more than 1 year); or (b) directly dried under vacuum at 80 °C overnight and stored in the glovebox (filled with N_2) for further use. The isolated yield was about 90~95% regarding the dry solid has the formula of $\text{CuB}_{12}\text{H}_{12}(\text{dpb})_2$ without any solvent molecules.

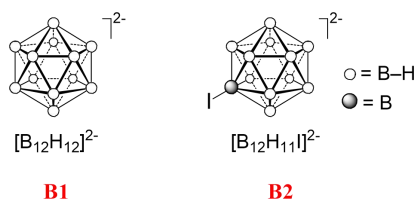
Preparation of single crystals: To a 4 mL long thin tube was added a 1 mL of aqueous solution with $[\text{Na}]_2[\text{B}_{12}\text{H}_{12}]$ (~ 2 mg) and $\text{Cu}[\text{NO}_3]_2 \cdot 3\text{H}_2\text{O}$ (~ 2 mg). 1 mL of MeOH/ H_2O mixture was slowly layered above the solution, followed by a 1 mL of MeOH solution of dpa (4 mg). The tube was sealed and left undisturbed at 298 K. After ~1 week, violet single crystals suitable for X-ray diffraction analysis were obtained.

Preparation of BSF-3-Co

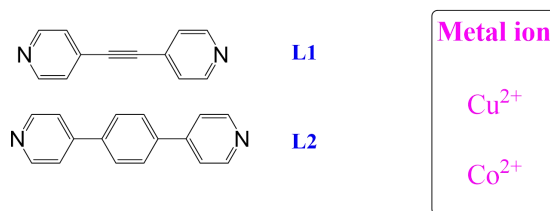
Bulky synthesis: A mixture of $[\text{Na}]_2[\text{B}_{12}\text{H}_{12}]$ (225 mg, 1.2 mmol, 1.2 equiv) and $\text{Co}[\text{NO}_3]_2 \cdot 6\text{H}_2\text{O}$ (291 mg, 1 mmol, 1 equiv) was dissolved in 10 mL of water in a 100 mL bottle and heated to 65 °C. Then a MeOH (40 mL) suspension of 1,4-di(pyridin-4-yl)benzene (dpa) (464 mg, 2 mmol, 2 equiv, almost dissolved) was slowly added to the above solution. The bottle was well sealed; pink solid formed at first, and the suspension was stirred at 65 °C for another 48 h to give yellow solid. The solid was then collected by filtration, washed by MeOH (10 mL), followed by: (a) soaked in anhydrous MeOH for further use (BSF-3-Co was stable in dry MeOH for more than 1 year); or (b) directly dried under vacuum at 80 °C overnight and stored in the glovebox (filled with N_2) for further use. The yield was about 80~85% based on that the dried product has the formula of $\text{CoB}_{12}\text{H}_{12}(\text{dpb})_2$ without any solvent molecules.



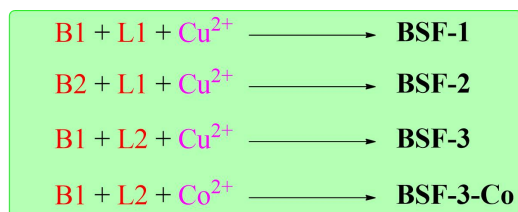
a) Studied boron cluster anions



b) Studied dipyrindyl ligands and metal ions



c) Reticular synthesis of BSFs



Scheme S1. Construction of boron-cage hybrid metal-organic supramolecular frameworks by self-assembly of cluster borates, dipyrindyl ligands and metal ions.

Single-crystal X-ray diffraction studies were conducted at 173 K on a BrukerAXS D8 VENTURE diffractometer equipped with a PHOTON-100/CMOS detector ($GaK\alpha$, $\lambda = 1.34139 \text{ \AA}$). Indexing was performed using APEX2. Data integration and reduction were completed using SaintPlus 6.01. Absorption correction was performed by the multi-scan method implemented in SADABS. The space group was determined using XPREP implemented in APEX2.1 The structure was solved with SHELXS-97 (direct methods) and refined on F2 (nonlinear least-squares method) with SHELXL-97 contained in APEX2, WinGX v1.70.01, and OLEX2 v1.1.5 program packages. All non-hydrogen atoms were refined anisotropically. The contribution of disordered solvent molecules was treated as diffuse using the Squeeze routine implemented in Platon.

Powder X-ray diffraction (PXRD) data were collected on a SHIMADZU XRD-6000 diffractometer ($Cu K\alpha\lambda = 1.540598 \text{ \AA}$) with an operating power of 40 KV, 30mA and a scan speed of $4.0^\circ/\text{min}$. The range of 2θ was from 5° to 50° .

Thermal gravimetric analysis was performed on a TGA Q500 V20.13 Build 39 instrument. Experiments were carried out using a platinum pan under nitrogen atmosphere which conducted by a flow rate of 60 mL/min nitrogen gas. First, the sample was heated at 80 °C for 1 h to remove the water residue and equilibrated for 5 minutes, then cooled down to 50 °C. The data were collected at the temperature range of 50 °C to 800 °C with a ramp of 10 °C /min.

The gas adsorption measurements were performed on a Micromeritics ASAP 2460 instrument. Before gas adsorption measurements, the sample was evacuated at 80 °C for 1 day until the pressure dropped below 7 µmHg. The sorption isotherms were collected at 273–313 K on activated samples.

Fitting of experimental data on pure component isotherms

As we know, the more parameters, the better fitting of the experimental data. However, the fitting should rationally describe the physical meaning of adsorbents and adsorbates. For all the MOFs for every single gas adsorption, the most complicated dual-site Langmuir-Freundlich model was applied at first. Then we simplified the parameters to dual-site Langmuir model or even 1-site Langmuir model in case the fitting accuracy is still excellent (correlation coefficient $R^2 > 0.995$)

The unary isotherm data for C₂H₂, C₂H₄, and CO₂ in BSF-1, BSF-2, BSF-3, BSF-3-Co, and TIFSIX-2-Ni-i were measured at 298 K, 273 K and 313 K. For all MOFs unless otherwise stated, the C₂H₂ unary isotherms were fitted using the dual-site Langmuir model with excellent accuracy.

$$q = q_{A,sat} \frac{b_A p}{1 + b_A p} + q_{B,sat} \frac{b_B p}{1 + b_B p} \quad (1)$$

The C₂H₄ unary isotherms for all MOFs at 273 K were amenable to fitting with the 1-site Langmuir model to excellent accuracy with

$$q = q_{sat} \frac{bp}{1 + bp} \quad (2)$$

The unary isotherm data for CO₂ in BSF-1, BSF-3, BSF-3-Co and TIFSIX-2-Ni-i could also fitted with very good accuracy with the 1-site Langmuir model.

However, the unary isotherm data for CO₂ in BSF-2 shows a distinct inflection characteristic and required fitting with the dual-site Langmuir-Freundlich model:

$$q = q_{A,sat} \frac{b_A P^{v_A}}{1 + b_A P^{v_A}} + q_{B,sat} \frac{b_B P^{v_B}}{1 + b_B P^{v_B}} \quad (3)$$

Here, P is the pressure of the bulk gas at equilibrium with the adsorbed phase (Pa), q is the adsorbed amount per mass of adsorbent (mol kg^{-1}), $q_{A,sat}$ and $q_{B,sat}$ are the saturation capacities of site A and B (mol kg^{-1}), b_A and b_B are the affinity coefficients of site A and B (Pa^{-v}), and v_A and v_B represent the deviations from an ideal homogeneous surface.

For analysis of the separations of $\text{C}_2\text{H}_2/\text{CO}_2$ mixtures using TIFSIX-2-Cu-i, JCM-1, and DICRO-4-Cu-i, the unary isotherm data fits for C_2H_2 , and CO_2 reported in the Supporting Material accompanying the original publications were used; the sources are specified below.

1) *TIFSIX-2-Cu-i: Dual-site Langmuir-Freundlich parameters in Figure S15, and S16 of Chen et al., Chem 1, 753–765*

2) *JCM-1: Dual-site Langmuir parameters in Table S3 of Lee et al. Angew. Chem. 2018, 130, 7995 –7999*

3) *DICRO-4-Cu-i: Dual-site Langmuir-Freundlich parameters in Figure S13, and S14 of Scott et al., ACS Appl. Mater. Interfaces 2017, 9, 33395–33400*

4) *MUF-17: Dual-site Langmuir parameters in Figure S13 of Chem. Mater. 2019, 31, 4919–4926*

The binding energy is reflected in the isosteric heat of adsorption, Q_{st} , defined as:

$$Q_{st} = RT^2 \left(\frac{\partial \ln p}{\partial T} \right)_q \quad (4)$$

The calculations are based on the use of the Clausius-Clapeyron equation.

IAST calculations of adsorption selectivity and uptake capacities:

We consider the separation of binary: 50/50 $\text{C}_2\text{H}_2/\text{C}_2\text{H}_4$, 1/99 $\text{C}_2\text{H}_2/\text{C}_2\text{H}_4$, 50/50 $\text{C}_2\text{H}_2/\text{CO}_2$, 2/1 $\text{C}_2\text{H}_2/\text{CO}_2$ mixtures in BSF-1, BSF-2, BSF-3 and BSF-3-Co at 298 K, and varying total pressures.

We also consider the separation of binary: $\text{C}_2\text{H}_2/\text{C}_2\text{H}_4$ mixtures of varying bulk gas phase compositions in BSF-3 and BSF-3-Co at 298 K and total pressure of 100 kPa, $\text{C}_2\text{H}_2/\text{CO}_2$ mixtures of varying bulk gas phase compositions in BSF-3 and BSF-3-Co, and TIFSIX-2-Ni-i at 298 K and total pressure of 100 kPa.

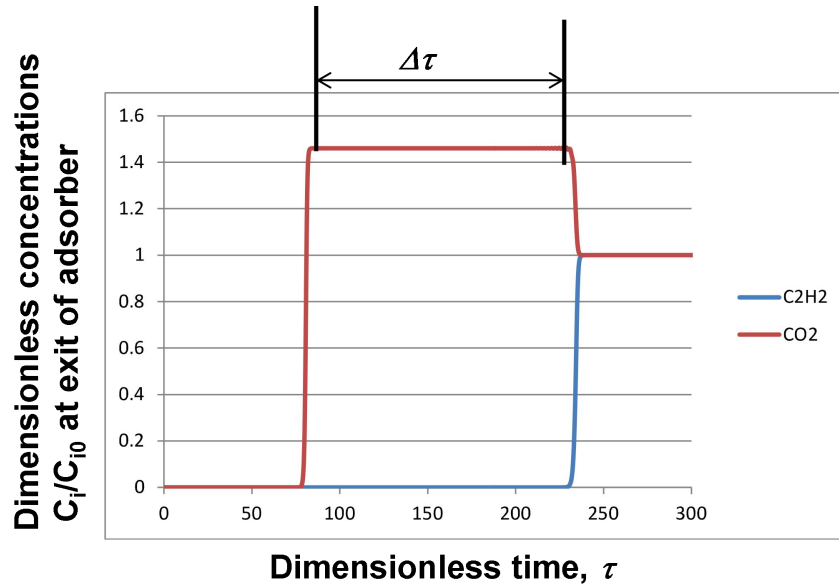
The IAST adsorption selectivity for two gases is defined as:

$$S_{ads} = \frac{q_1/q_2}{p_1/p_2} \quad (5)$$

q_1 , and q_2 are the molar loadings in the adsorbed phase in equilibrium with the bulk gas phase with partial pressures p_1 , and p_2 .

Transient breakthrough simulations

Transient breakthrough simulations were carried out for binary 50/50 C₂H₂/CO₂ mixtures in BSF-1, BSF-2, BSF-3, TIFSIX-2-Ni-i, TIFSIX-2-Cu-i, JCM-1, and DICRO-4-Cu-i, operating at a total pressure of 100 kPa and 298 K, using the methodology described in earlier publications.² For the breakthrough simulations, the following parameter values were used: length of packed bed, $L = 0.3$ m; voidage of packed bed, $\varepsilon = 0.4$; superficial gas velocity at inlet, $u = 0.04$ m/s. The x -axis is the *dimensionless* time, $\tau = t \times u / (L \times \varepsilon)$, defined by dividing the actual time, t , by the characteristic time, $L\varepsilon/u$.



The breakthrough simulations demonstrate the potential of separating C₂H₂ from CO₂ during a certain time interval $\Delta\tau$.

Separation potential calculation

The separation performance in fixed bed adsorbers is dictated not only by selectivity, but also the uptake capacity. For this reason, a combined metric, called the separation potential, was introduced recently by Krishna.^{2a,b} This combined metric Δq , represents the difference of moles of component 1 (the more strongly adsorbed

species) and component 2 (the less strongly adsorbed species) adsorbed in the per kg of adsorbent in the fixed bed.

$$\Delta q = q_1 \frac{y_2}{y_1} - q_2 \quad (6)$$

where q_1 , q_2 are the molar loading (units: mol/kg) for mixture adsorption, calculated from the IAST or breakthrough simulation. The values of Δq_{IAST} were determined from IAST calculation. The values of Δq_{break} were determined from a rigorous material balance performed for each of the breakthrough simulations to determine the component uptakes.

For comparing the performance of BSFs and other leading MOFs, the Δq_{IAST} and Δq_{break} were all calculated for them.

It is noteworthy that for all MOFs, the Δq_{break} in the fixed bed adsorber is lower than the corresponding Δq_{IAST} value because of the distended nature of the breakthroughs in the fixed bed.

The breakthrough experiments were carried out in a dynamic gas breakthrough equipment. The experiments were conducted using a stainless steel column (10 mm inner diameter \times 100 length or 4.9 mm inner diameter \times 100 length). The weight of and BSF-1 and BSF-3 packed in the column (Φ 4.9 mm \times 100 mm) was 2.13 g and 1.98 g, respectively. The weight of BSF-3 packed in the column (Φ 4.9 mm \times 100 mm) was 0.47 g. The column packed with sample was first purged with a N_2 flow (10 mL min^{-1}) for 12 h at 75 °C. The mixed gas of $\text{C}_2\text{H}_2/\text{CO}_2/\text{He}$ (10/5/85, v/v/v), $\text{C}_2\text{H}_2/\text{CO}_2$ (50/50, v/v/v) was then introduced to BSF-3 or BSF-1. Outlet gas from the column was monitored using gas chromatography (GC-490) with the thermal conductivity detector TCD. After the breakthrough experiment, the sample was usually regenerated with a N_2 flow of 5 mL min^{-1} under 45~80 °C for 8 ~16 h. The actual flow rate of the mixed gas was determined by self-designed soap film volumetric flowmeter due to the fact the commercial mass flowmeter we used in the experiments was not able to reflect the real flow rate of the mixed gas. The real volumetric flow rate determined in this work for BSF-1 and BSF-3 is slightly different although the values shown in the mass flowmeter are the same.

Calculation of separation factor (α)

The amount of gas adsorbed i (q_i) is calculated from the breakthrough curve using the following:

$$q_i = \frac{V_T P_i \Delta T}{m} \quad (7)$$

Here, V_T is the total flow rate of gas (cm^3/min), P_i is the partial pressure of gas i (atm), ΔT is the time for initial breakthrough of gas i to occur (mins) and m is the mass of the sorbent (g). The separation factor (α) of the breakthrough experiment is determined as

$$\alpha = \frac{q_1 y_2}{q_2 y_1} \quad (8)$$

Where, y_i is the partial pressure of gas i in the gas mixture.

Grand canonical Monte Carlo (GCMC) simulations were performed in MS 2017R2 package using sorption module. The structure of BSF-3 was from the single crystal structure after modifying the disordered atoms. The frameworks were considered to be rigid during the GCMC simulation. The interaction between gas and frameworks were computed through the Coulomb and Lennard-Jones 6-12 (LJ) potentials. The LJ parameters of framework atoms were taken from the universal force field (UFF), and the partial charges were described by the QEq charge distribution method. The C_2H_2 model were taken from Yuan et al. (Nat. Commun. 2015, 6, 7515). The cutoff radius was chosen 18.5 Å for Van der Walls interaction and the long range electrostatic interactions were handled using the Ewald summation method. The loading steps and the equilibration steps were 1×10^7 , the production steps were 1×10^7 .

The density functional theory (DFT) calculations were performed using the Gaussian 09 package. The PBE0 functionals with the Grimme's D3(BJ) dispersion correction were applied to DFT calculations along with the 6-311+G(d,p) basis set. As the periodic structure of BSF-3 is too large for the DFT calculations, one or two $\text{B}_{12}\text{H}_{12}^{2-}$ cluster were isolated from the periodic structure (based on the GCMC simulation results) to calculate the interactions of C_2H_2 , C_2H_4 and CO_2 with BSF-3. All structures were optimized without any symmetry constraints and the optimized minimum-energy structures were verified as stationary points on the potential energy surface by performing numerical harmonic vibrational frequency calculations. Specify, for two $\text{B}_{12}\text{H}_{12}^{2-}$ cluster model, the cluster B and H atoms were held fixed throughout the simulations to describe the position of boron cluster in pore II. The equation for the calculation of binding energy (ΔE) is defined as: $\Delta E = E(\text{BSF-3+gas}) - [E(\text{BSF-3}) + E(\text{gas})]$.

To investigate the effect of distance between two $[\text{B}_{12}\text{H}_{12}]^{2-}$ anions on C_2H_2 adsorption, we calculated the potential energy curves for one C_2H_2 molecule and two $[\text{B}_{12}\text{H}_{12}]^{2-}$ anions with Gaussian 09 package using a PBE0 level of theory and def2-SVP basis set. We first constructed several configurations with the distance between the center of two $[\text{B}_{12}\text{H}_{12}]^{2-}$ clusters ranged from 11.0 to 13.5 Å, and then a C_2H_2 molecule was placed in the between the two $[\text{B}_{12}\text{H}_{12}]^{2-}$ clusters. The Geometry optimization was performed for every configuration, and the intermolecular binding energies between C_2H_2 and two $[\text{B}_{12}\text{H}_{12}]^{2-}$ anions were calculated. In all calculations, the atom positions of $[\text{B}_{12}\text{H}_{12}]^{2-}$ clusters were considered constrained, and the C_2H_2 was kept relaxed. This method is also applied to calculate the binding energies between C_2H_2 and two $[\text{B}_{12}\text{H}_{12}]^{2-}$ anions by varying the $\text{H}(\text{B})\cdots\text{H}(\text{B})$ distances.

The theoretical surface area calculation was performed using the Zeo++ package.

II. Characterization (X-ray Crystallography Data, IR, TGA and EPR)

Table S1. Single crystal data of BSF-1, BSF-2 and BSF-3.

	BSF-1	BSF-2	BSF-3
Cell	a=28.764(2) b=17.1839(11) c=19.918(3) $\alpha=90$ $\beta=133.107(2)$ $\gamma=90$	a=28.398(2) b = 17.7840(12) c = 20.2046(15) $\alpha= 90$ $\beta= 133.929(2)$ $\gamma = 90$	a=19.8856(17) b=22.4095(18) c=21.0263(16) $\alpha=90$ $\beta=90$ $\gamma=90$
Temperature	173 K	173(2) K	193 K
Volume (\AA^3)	7187.6(13)	7348.9(10)	9369.9(13)
Space group	C 2/c	C2/c	Ima2
Hall group	-C2yc	-C2yc	I2-2a
formula	$\text{C}_{24}\text{H}_{28}\text{B}_{12}\text{CuN}_4$	$\text{C}_{24}\text{H}_{27}\text{B}_{12}\text{CuIN}_4$	$\text{C}_{32}\text{H}_{36}\text{B}_{12}\text{CuN}_4$
Molecular weight	565.77	691.65	669.91
density	1.046	1.250	0.95
Z	8	8	8
R	0.0684	0.1525	0.0912
wR2	0.1859	0.3725	0.2616
S	1.043	1.150	1.121

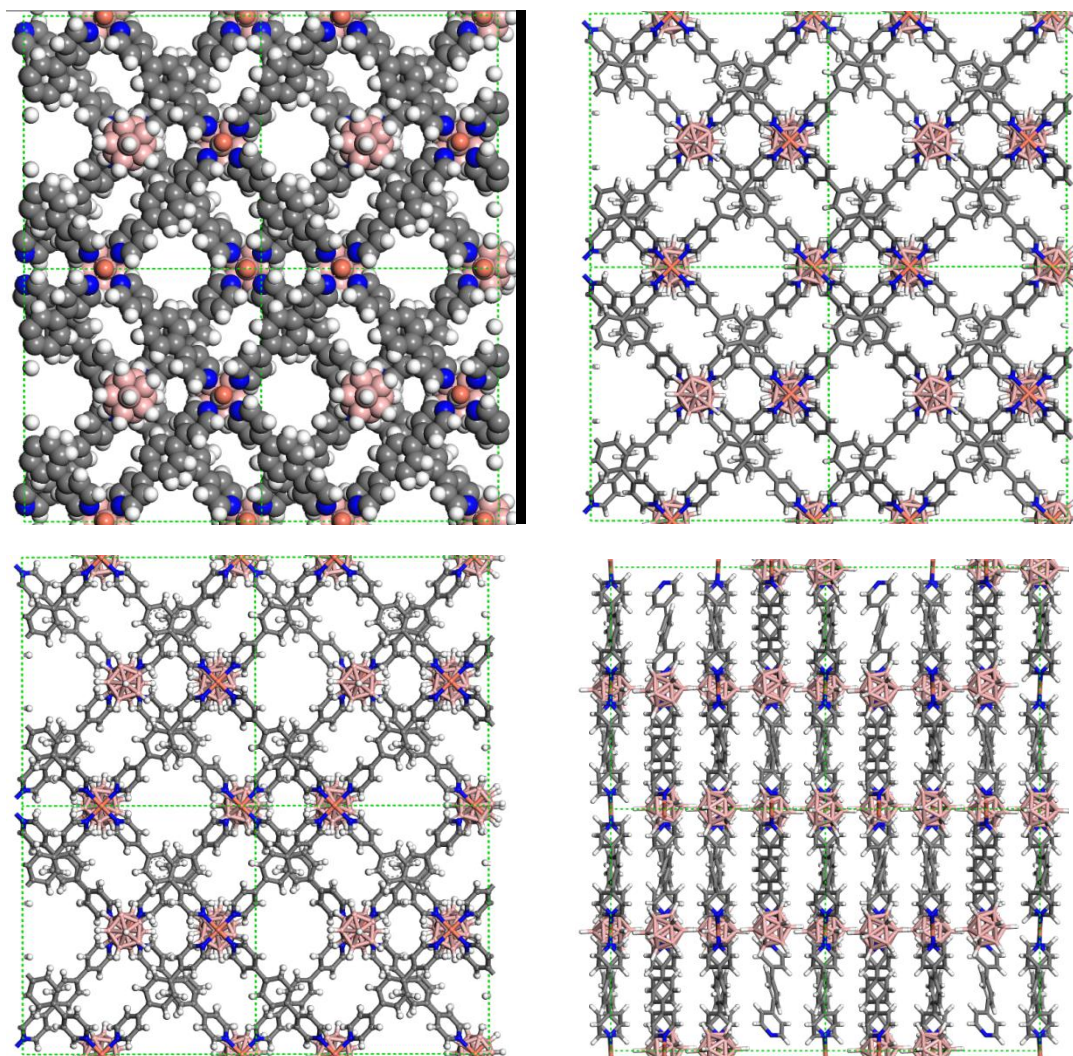


Figure S1. $2 \times 2 \times 2$ packing diagrams of BSF-3 viewed down the crystallographic a -axis in space-fill mode (top left), stick mode (top right) and ball-stick mode (down left). Aligned dodecaborates can be observed when viewed down the crystallographic c -axis (down right)

■

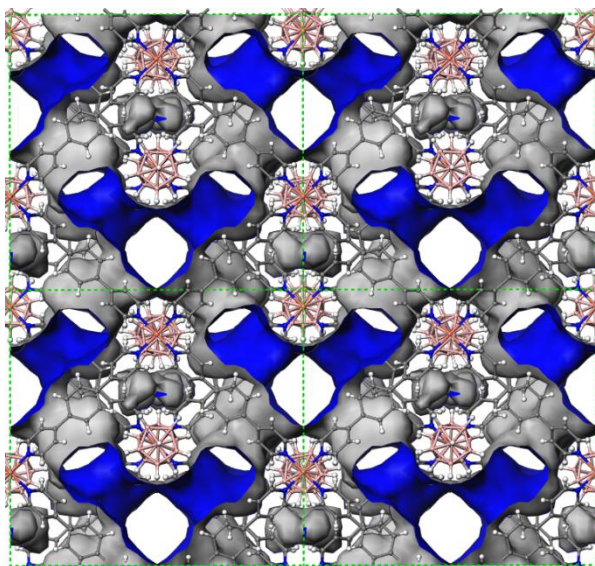


Figure S2. $2 \times 2 \times 2$ packing diagrams of BSF-3 viewed down the crystallographic *a*-axis in ball-stick mode with void surface in blue determined using a probe of 1.2 Å by PLATON.

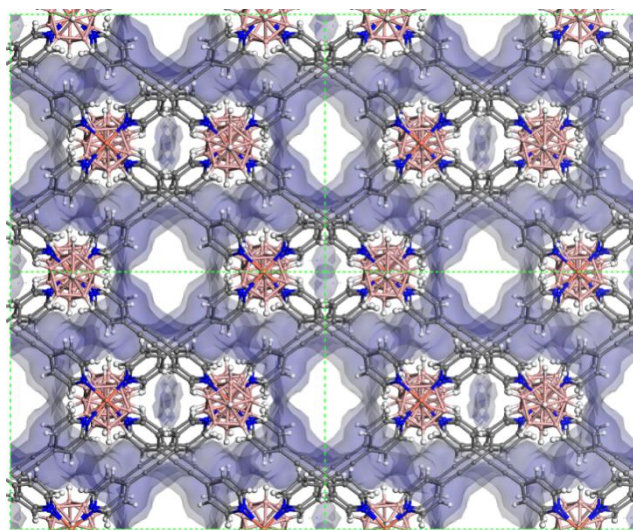


Figure S3. $2 \times 2 \times 2$ packing diagrams of BSF-1 viewed down the crystallographic *c*-axis in ball-stick mode with void surface in light blue determined using a probe of 1.2 Å by PLATON.

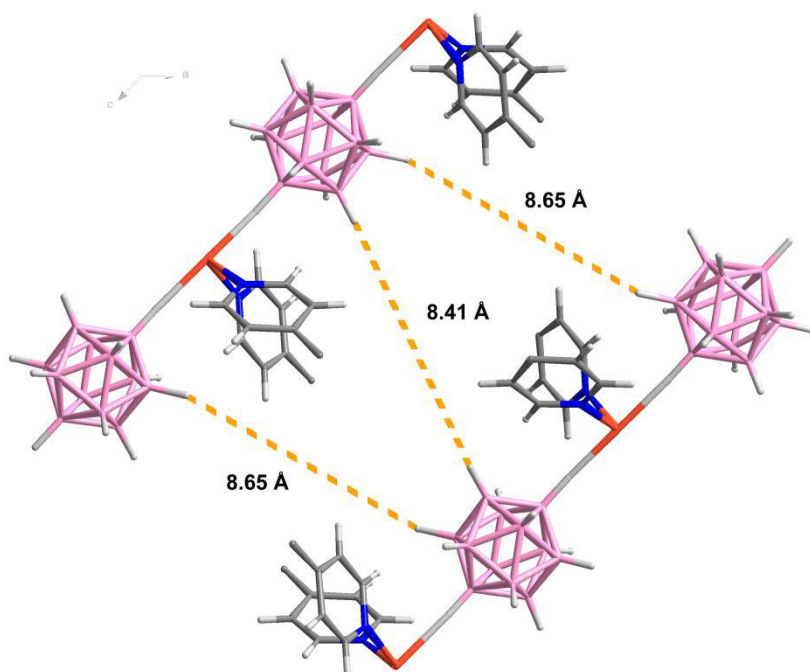


Figure S4. Opposite H(B)···H(B) distance within the largest pore of BSF-1

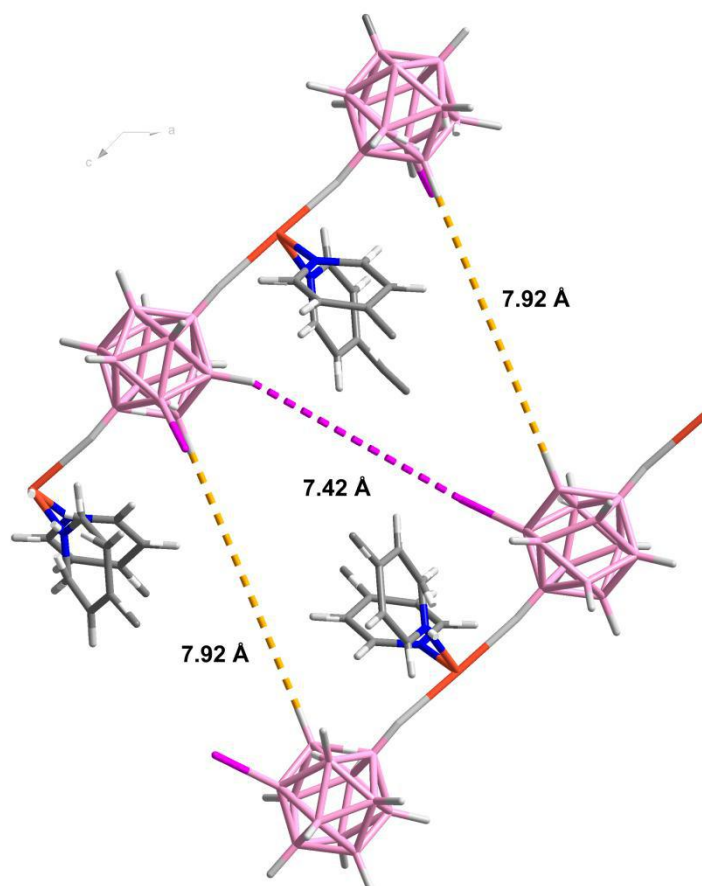


Figure S5. Opposite H(B)···H(B) distance within the largest pore of BSF-2.

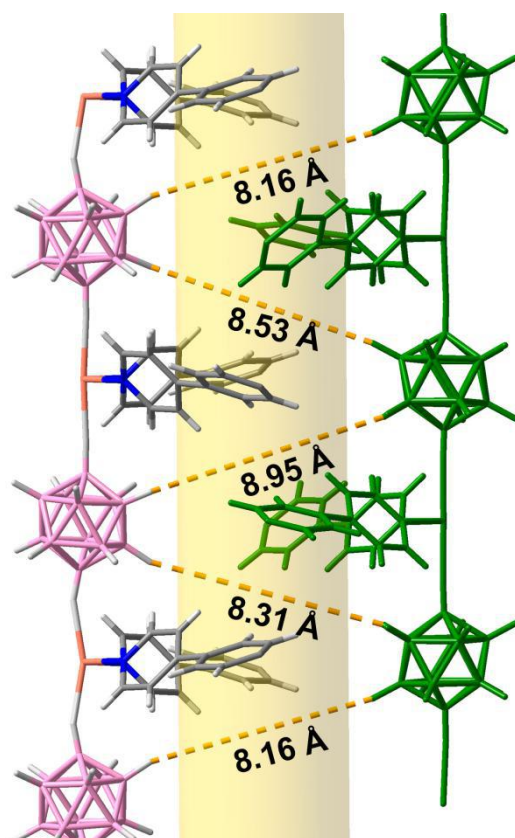


Figure S6. Opposite H(B)···H(B) distance within the largest pore (Pore I) of BSF-3.

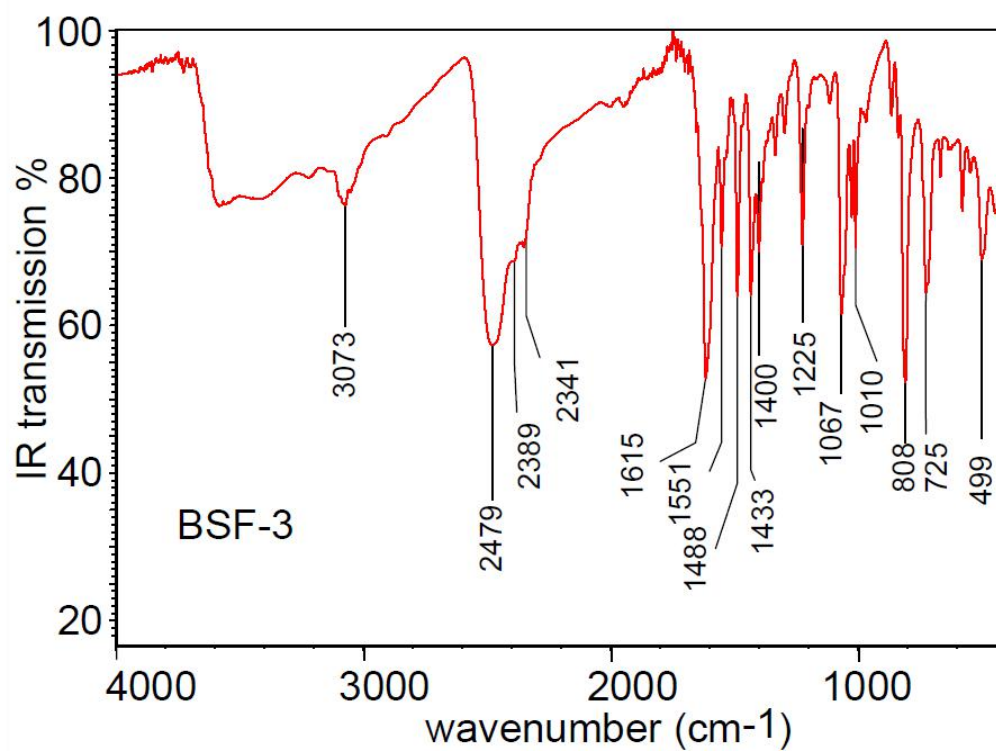


Figure S7. IR spectrum of dry BSF-3

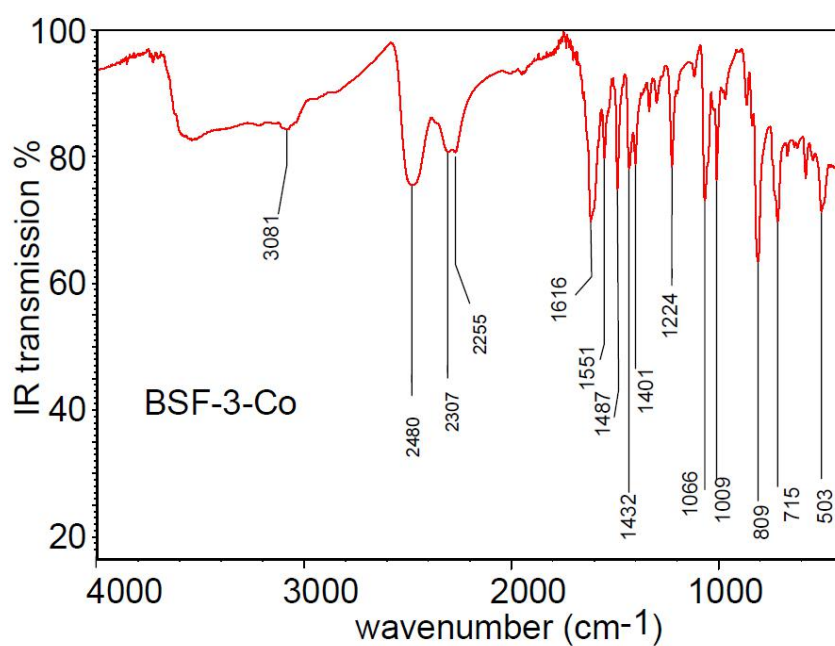


Figure S8. IR spectrum of dry BSF-3-Co.

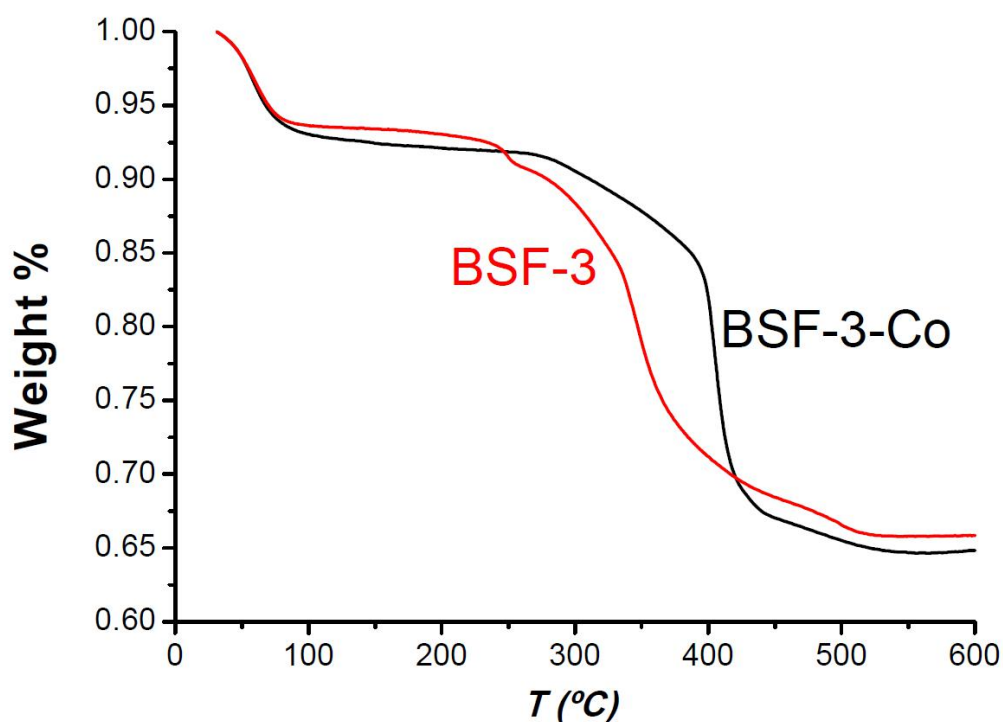


Figure S9. TGA curves of fresh BSF-3 and BSF-3-Co. The weight loss between 50-100 °C is because of the loss of MeOH and water from the sample. The weights keep consistent until ~250 °C for BSF-3 and ~270 °C for BSF-3-Co. BSF-3-Co is relatively more thermally stable.

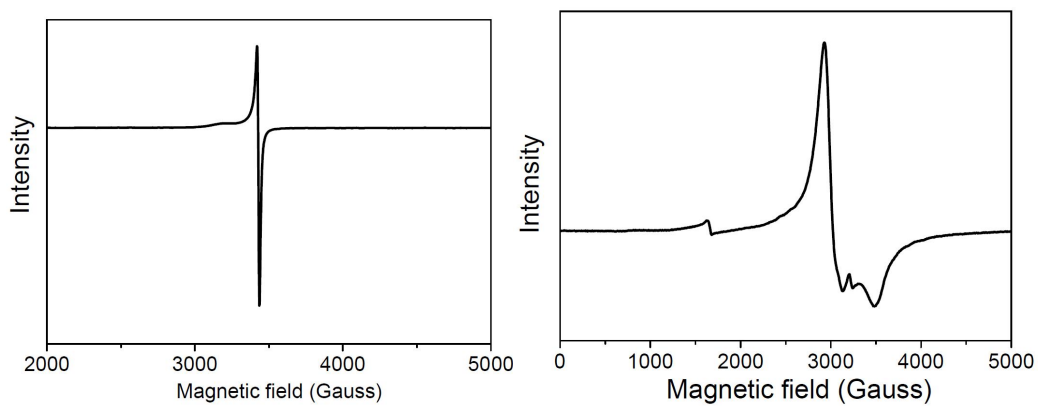
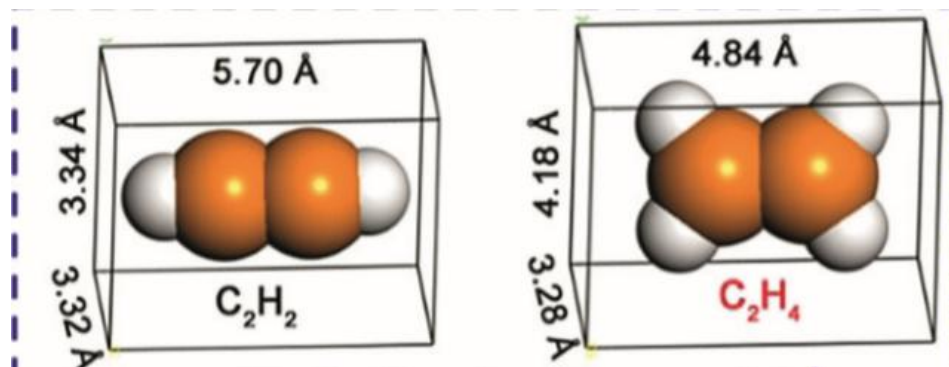


Figure S10. EPR spectrum of BSF-3 (left) and BSF-3-Co (right) indicates the oxidation state of metal is Cu(II) and Co(II), respectively.

III. Adsorption data, IAST selectivity and Q_{st}

Table S2. Comparison of C_2H_2 , C_2H_4 and CO_2

Gas molecules	Dynamic Size (Å)	Molecular size (Å ³)	Boiling point (K)	Quadrupole Moment (C m ²)
C_2H_2	3.3	3.32 x 3.34 x 5.70	189.3	20.5×10^{-40}
CO_2	3.3	3.18 x 3.33 x 5.36	194.7	-13.4×10^{-40}
C_2H_4	4.163	3.28 x 4.18 x 4.84	169.5	



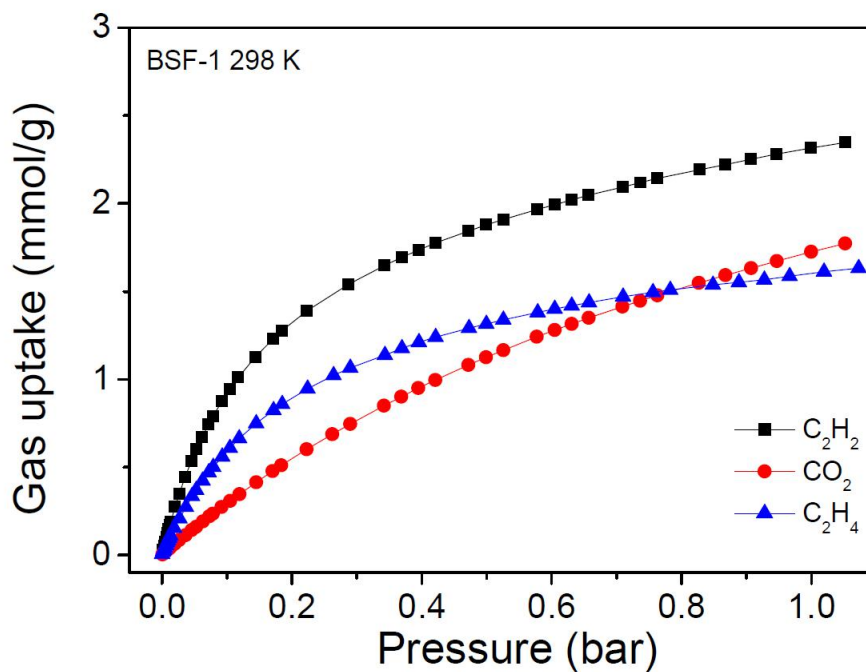


Figure S12. C₂H₂, CO₂ and C₂H₄ adsorption isotherms on BSF-1 at 298 K

Table S3. Unary isotherm fit parameters C₂H₂ ($R^2 = 0.99997$), C₂H₄ ($R^2 = 0.9996$), and CO₂ ($R^2 = 0.99999$) in BSF-1 at 298 K.

	Site A			Site B		
	$q_{A,sat}$ mol kg ⁻¹	b_A Pa ^{-v_A}	v_A dimensionless	$q_{B,sat}$ mol kg ⁻¹	b_B Pa ^{-v_B}	v_B dimensionless
C ₂ H ₂	1.7	8.73425E-05	1	1.9	7.07024E-06	1
C ₂ H ₄	1.9	4.62567E-05	1			
CO ₂	3.5	9.55E-06	1			

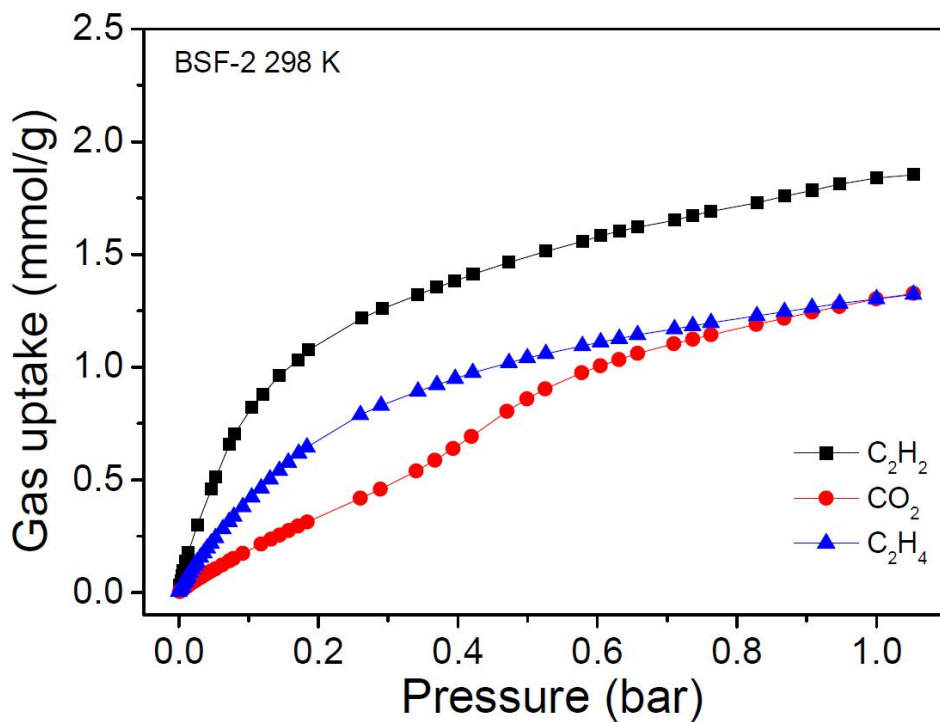


Figure S13. C₂H₂, CO₂ and C₂H₄ adsorption isotherms on BSF-2 at 298 K

Table S4. Unary isotherm fit parameters for C₂H₂ ($R^2 = 0.9999$), C₂H₄ ($R^2 = 0.998$), and CO₂ ($R^2 = 0.999$) in BSF-2 at 298 K.

	Site A			Site B		
	$q_{A,sat}$ mol kg ⁻¹	b_A Pa ^{-ν_A}	ν_A dimensionless	$q_{B,sat}$ mol kg ⁻¹	b_{B0} Pa ^{-ν_B}	ν_B dimensionless
C ₂ H ₂	1.5	9.71802E-05	1	3.3	1.65129E-06	1
C ₂ H ₄	1.7	3.21694E-05	1			
CO ₂	0.82	1.38862E-16	3.37	0.69	3.6154E-05	1

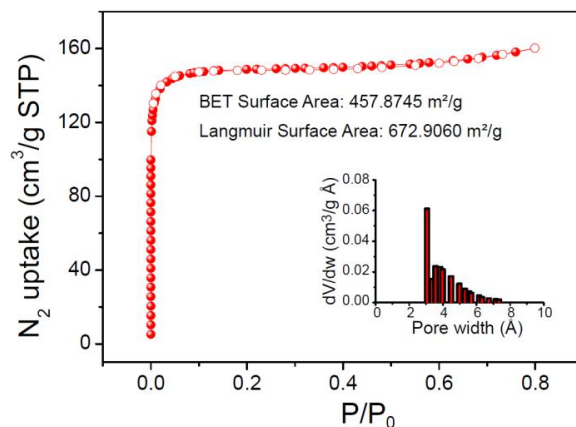


Figure S14. The N_2 sorption isotherm on BSF-3 at 77 K and calculated pore size distribution. The experimental BET surface area was ~ 457 m^2/g , close to the theoretical surface area of 513.197 m^2/g calculated by Zeo++.

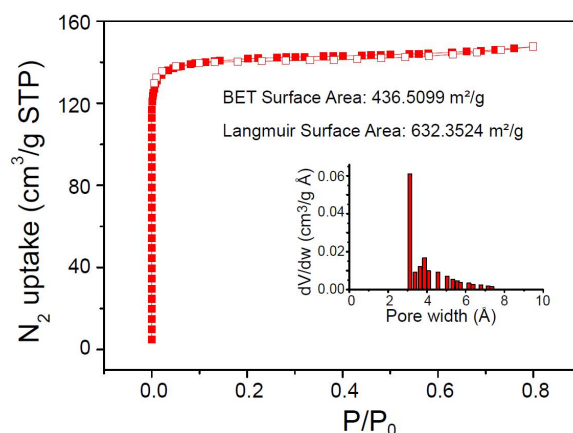


Figure S15. The N_2 sorption isotherm on BSF-3-Co at 77 K and calculated pore size distribution.

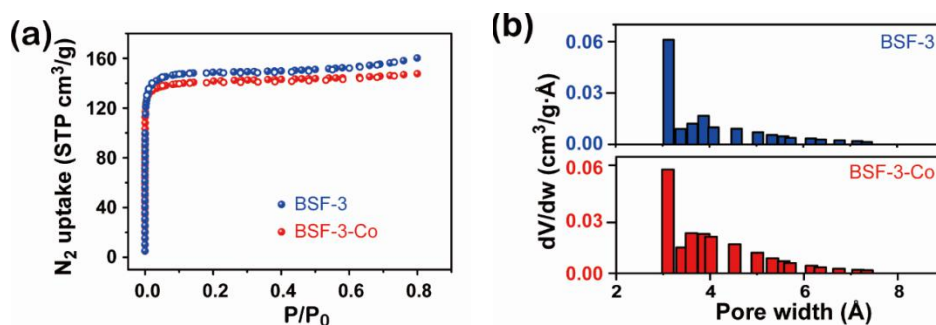


Figure S16. Comparison of the N_2 sorption isotherms and calculated pore size distribution on BSF-3 and BSF-3-Co at 77 K.

Pore volume analysis: single component N_2 adsorption at 77 K indicated that BSF-3 and BSF-3-Co has a maximum pore volume of 0.24 cm^3/g and 0.22 cm^3/g at

$P/P_0 = 0.15$, respectively, close to the calculated pore volume of BSF-3 ($0.29 \text{ cm}^3/\text{g}$) from its single crystal structure.

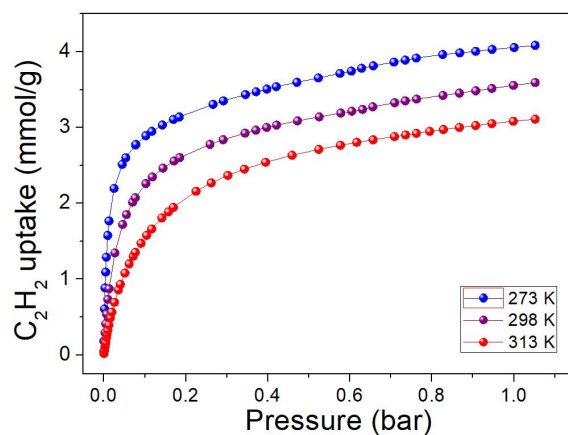


Figure S17. Adsorption isotherms of C_2H_2 on BSF-3 at temperature from 273 to 313 K.

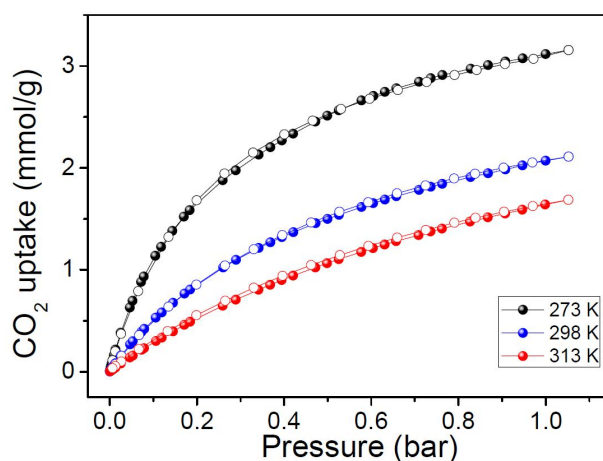


Figure S18. Sorption isotherms of CO_2 on BSF-3 at temperature from 273 to 313 K.

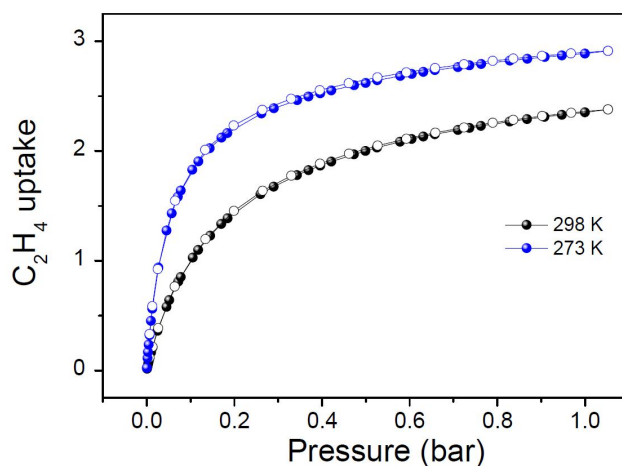


Figure S19. Sorption isotherms of C_2H_4 on BSF-3 at 273 K and 298 K.

Table S5. Unary isotherm fit parameters for C₂H₂ ($R^2 = 0.9999$), C₂H₄ ($R^2 = 0.9996$), and CO₂ ($R^2 = 0.9997$) in BSF-3 at 298 K.

	Site A			Site B		
	$q_{A,sat}$ mol kg ⁻¹	b_A Pa ^{-ν_A}	ν_A dimensionless	$q_{B,sat}$ mol kg ⁻¹	b_B Pa ^{-ν_B}	ν_B dimensionless
C ₂ H ₂	1.7	8.73425E-05	1	1.9	7.07024E-06	1
C ₂ H ₄	2.7	6.00E-05	1			
CO ₂	3	2.06E-05	1			

Table S6. Unary isotherm fit parameters for C₂H₂ ($R^2 = 0.9999$), C₂H₄ ($R^2 = 0.999$), and CO₂ ($R^2 = 0.9995$) in BSF-3 at 273 K.

	Site A			Site B		
	$q_{A,sat}$ mol kg ⁻¹	b_A Pa ^{-ν_A}	ν_A dimensionless	$q_{B,sat}$ mol kg ⁻¹	b_B Pa ^{-ν_B}	ν_B dimensionless
C ₂ H ₂	2.28	1.29E-05	1	2.8	0.001348	1
C ₂ H ₄	3	1.52E-04	1			
CO ₂	4.04	3.47E-05	1			

Table S7. Unary isotherm fit parameters for C₂H₂ ($R^2 = 0.9999$), and CO₂ ($R^2 = 0.99999$) in BSF-3 at 313 K.

	Site A			Site B		
	$q_{A,sat}$ mol kg ⁻¹	b_A Pa ^{-ν_A}	ν_A dimensionless	$q_{B,sat}$ mol kg ⁻¹	b_B Pa ^{-ν_B}	ν_B dimensionless
C ₂ H ₂	1.87	2.70E-05	1	1.795	1.78016E-4	1
CO ₂	3.518	8.718 E-5	1			

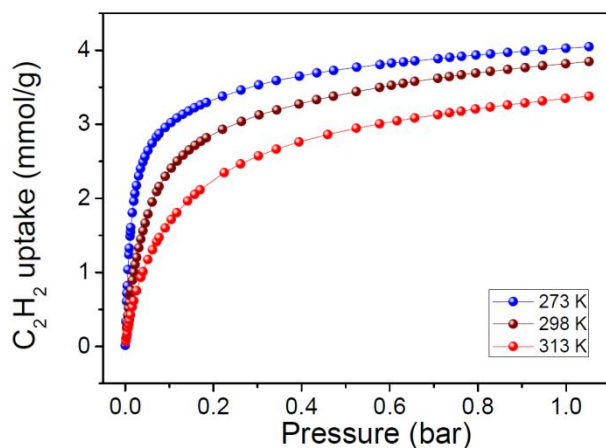


Figure S20. Adsorption isotherms of C_2H_2 on BSF-3-Co at temperature from 273 to 313 K.

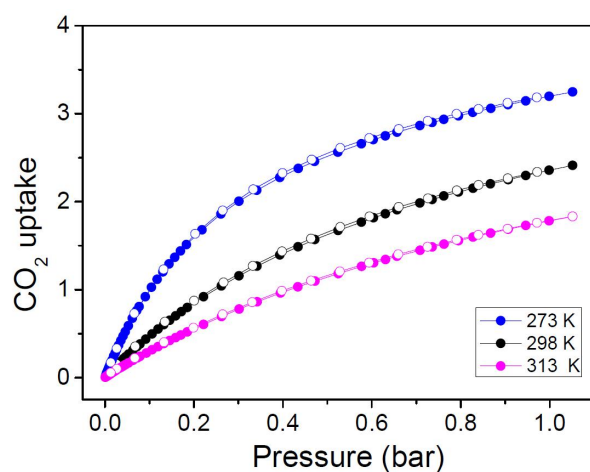


Figure S21. Sorption isotherms of CO_2 on BSF-3-Co at temperature from 273 to 313 K.

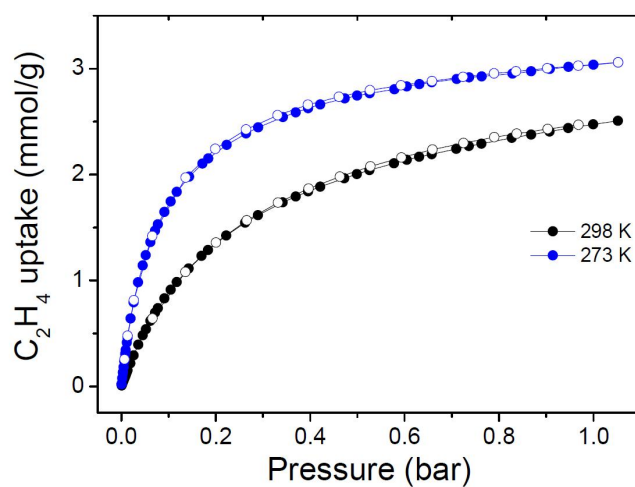


Figure S22. Sorption isotherms of C_2H_4 on BSF-3-Co at temperature at 273 and 298 K

Table S8. Unary isotherm fit parameters for C₂H₂ ($R^2 = 0.9999$), C₂H₄ ($R^2 = 0.9997$), and CO₂ ($R^2 = 0.99999$) in BSF-3-Co at 298 K.

	Site A			Site B		
	$q_{A,sat}$ mol kg ⁻¹	b_A Pa ^{-ν_A}	ν_A dimensionless	$q_{B,sat}$ mol kg ⁻¹	b_B Pa ^{-ν_B}	ν_B dimensionless
C ₂ H ₂	2.4	4.18E-04	1	1.9	3.31748E-05	1
C ₂ H ₄	3.05	3.96727E-05	1			
CO ₂	4.2	1.27065E-05	1			

Table S9. Unary isotherm fit parameters for C₂H₂ ($R^2 = 0.9999$), C₂H₄ ($R^2 = 0.9998$), and CO₂ ($R^2 = 0.9999$) in BSF-3-Co at 273 K.

	Site A			Site B		
	$q_{A,sat}$ mol kg ⁻¹	b_A Pa ^{-ν_A}	ν_A dimensionless	$q_{B,sat}$ mol kg ⁻¹	b_B Pa ^{-ν_B}	ν_B dimensionless
C ₂ H ₂	1.43	1.46E-05	1	3.22	7.33E-04	1
C ₂ H ₄	3.246	1.138E-04	1			
CO ₂	4.208	3.042E-05	1			

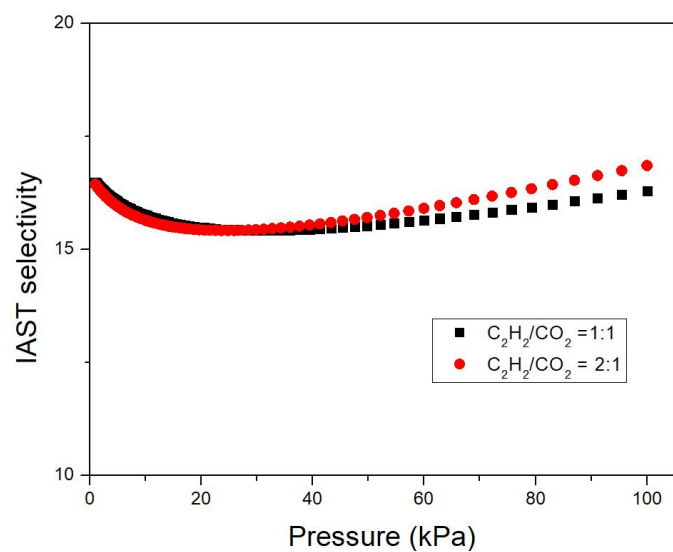


Figure S23. IAST adsorption selectivity of BSF-3 toward a C_2H_2/CO_2 (1:1 and 2:1) mixture at 298 K.

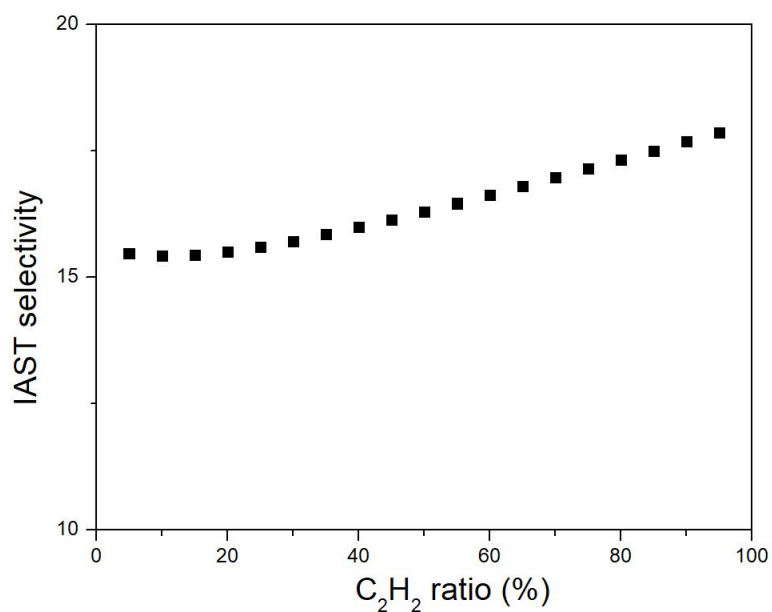


Figure S24. IAST adsorption selectivity of BSF-3 toward C_2H_2/CO_2 gas mixtures with different compositions at 298 K and 100 kPa.

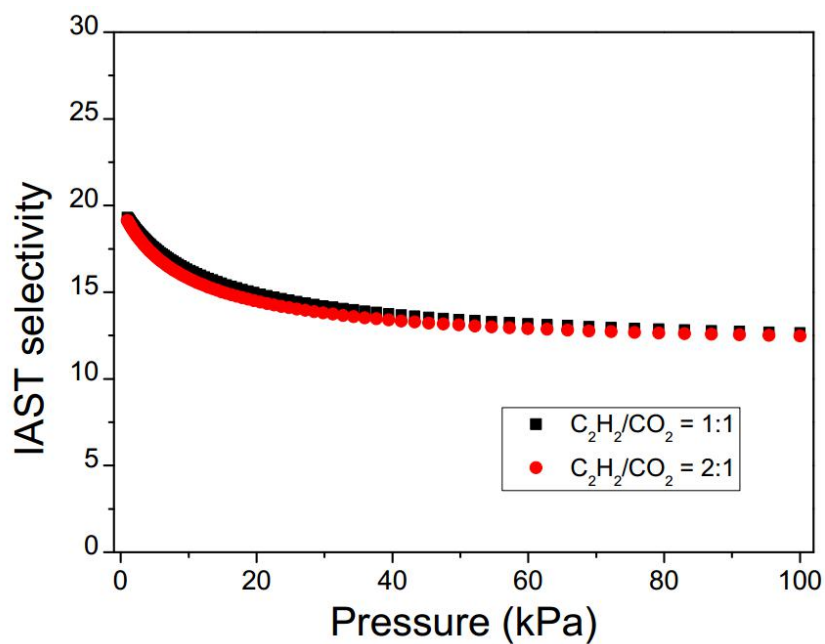


Figure S25. IAST adsorption selectivity of BSF-3-Co toward a C_2H_2/CO_2 (1:1 and 2:1) mixture at 298 K.

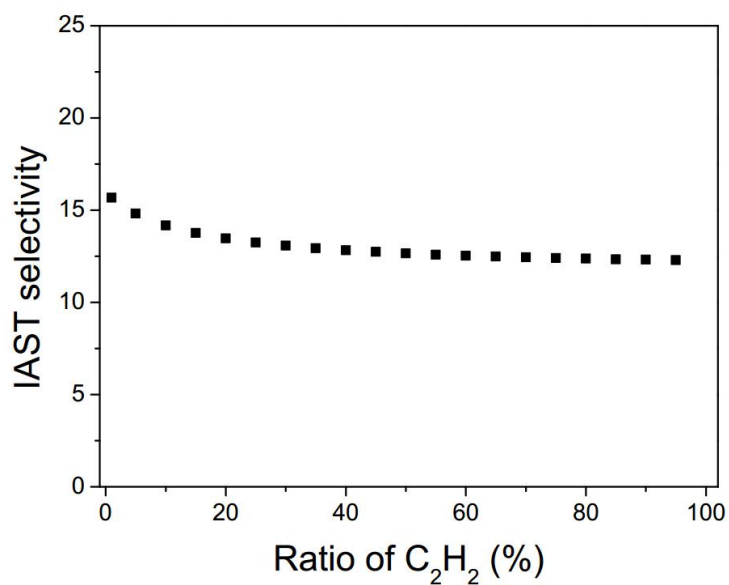


Figure S26. IAST adsorption selectivity of BSF-3-Co toward C_2H_2/CO_2 gas mixtures with different compositions at 298 K and 100 kPa.

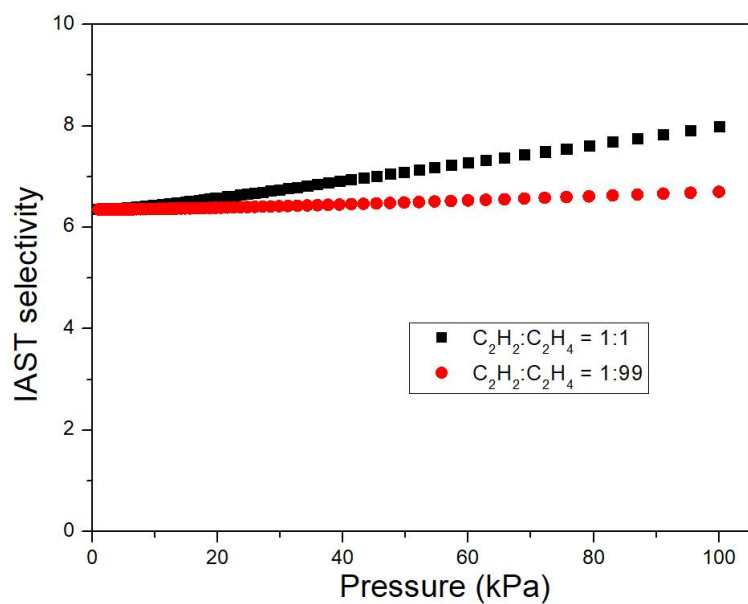


Figure S27. IAST adsorption selectivity of BSF-3 toward a C_2H_2/C_2H_4 (1:1 and 1:99) mixture at 298 K.

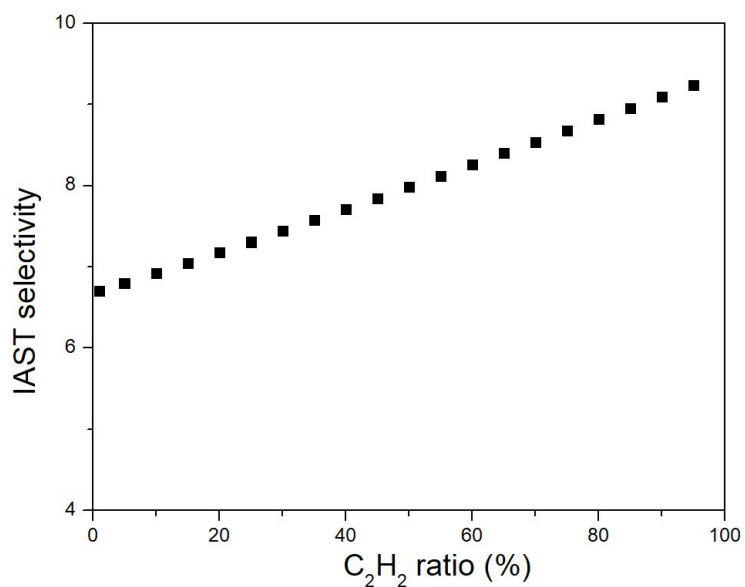


Figure S28. IAST adsorption selectivity of BSF-3 toward C_2H_2/C_2H_4 gas mixtures with different compositions at 298 K and 100 kPa.

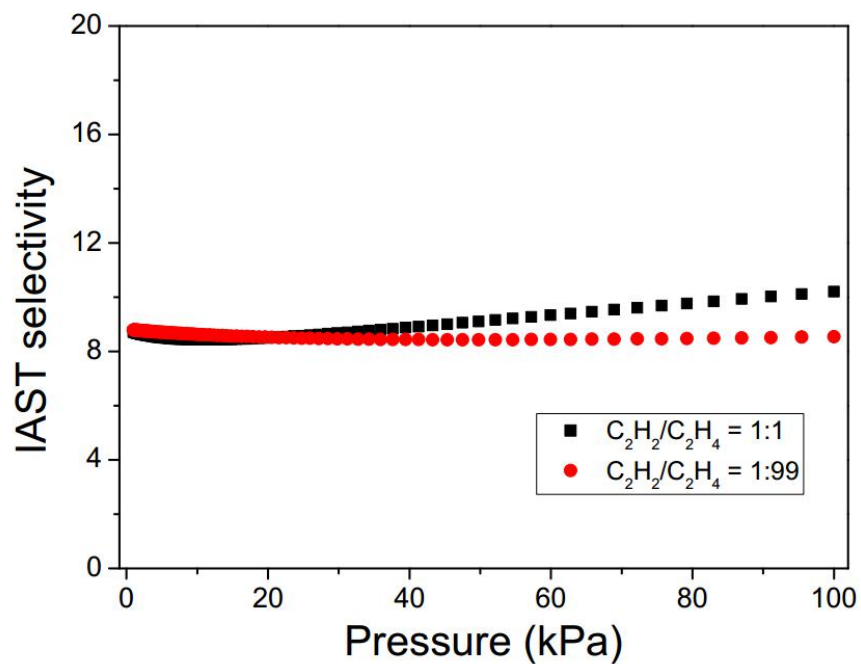


Figure S29. IAST adsorption selectivity of BSF-3-Co toward a C_2H_2/C_2H_4 (1:1 and 1:99) mixture at 298 K.

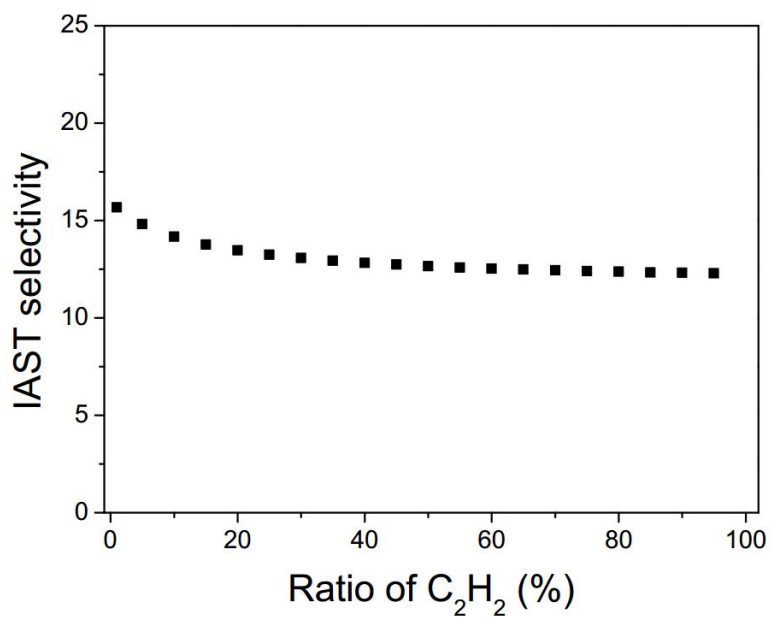


Figure S30. IAST adsorption selectivity of BSF-3-Co toward C_2H_2/C_2H_4 gas mixtures with different compositions at 298 K and 100 kPa.

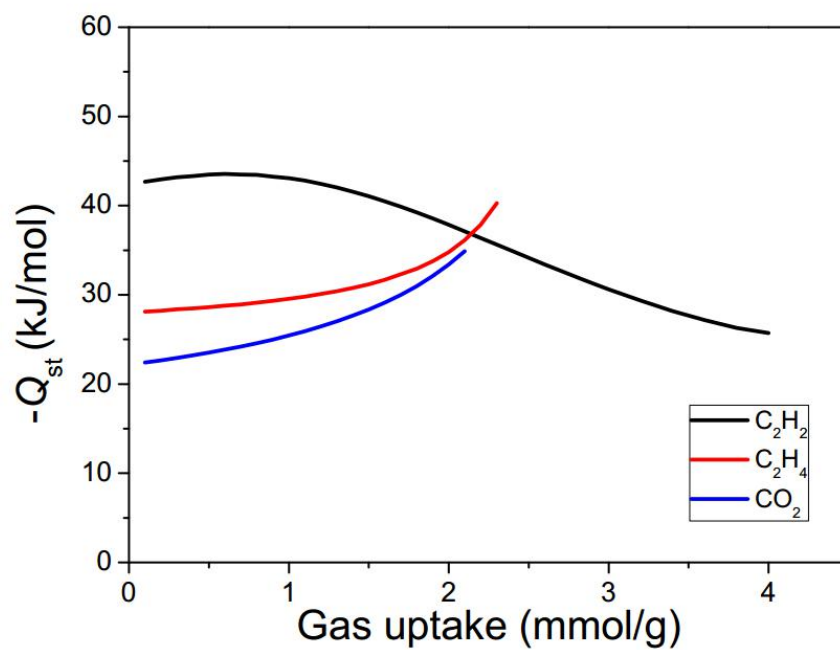
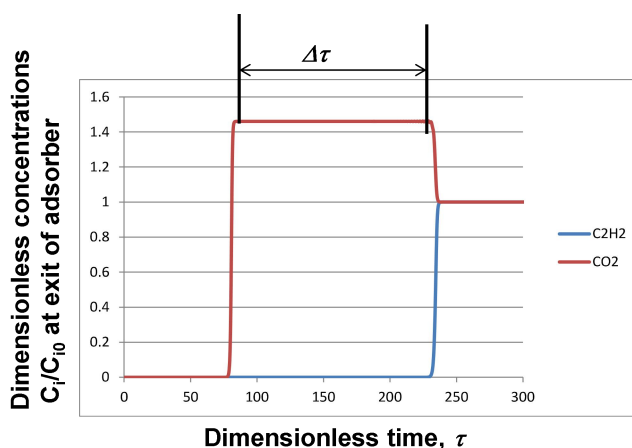


Figure S31. Q_{st} of BSF-3 toward C_2H_2 , C_2H_4 and CO_2 . The Q_{st} of BSF-3 for C_2H_2 , C_2H_4 and CO_2 adsorption are -42.7, -28.1 and -22.4 kJ/mol respectively at near-zero loadings. The increased $-Q_{st}$ with the gas adsorption for C_2H_4 and CO_2 indicates the enhanced gas – gas molecular interactions.

IV Breakthrough simulation

Transient breakthrough simulations were also carried out for binary 50/50 C₂H₂/CO₂ mixtures in BSF-1, BSF-2, BSF-3, TIFSIX-2-Ni-i, TIFSIX-2-Cu-i, JCM-1, DICRO-4-Cu-i and MUF-17, operating at a total pressure of 100 kPa and 298 K. The results are presented in Figure S35-42. The $\Delta\tau$, Δq_{IAST} and Δq_{break} were summarized below, which also indicate that BSF-3 has the best separation ability. Generally speaking, the larger the capacity difference (Δq_{break}), the better separation performance the material has.



Materials	$\Delta\tau$	Separation potential based on IAST calculation Δq_{IAST} (mol/kg)	Separation potential in the fixed bed Δq_{break} (mol/kg)
BSF-1	48.93	1.14	0.96
BSF-2	52.65	1.04	0.88
BSF-3	112.85	2.78	2.44
BSF-3-Co	-	3.01	~2.7*
TIFSIX-2-Ni-i	92.02	2.36	1.95
TIFSIX-2-Cu-i	100.44	2.58	2.18
JCM-1	145.27	2.43	2.12
DICRO-4-Cu-i	75.74	1.43	1.26
MUF-17	133.63	2.10	1.79

Table S10. Summarized $\Delta\tau$, Δq_{IAST} and Δq_{break} values of representative materials for separation of binary 50/50 C₂H₂/CO₂ mixtures. (*:supposed from the linear relationship in Figure 4c between Δq_{IAST} and Δq_{break})

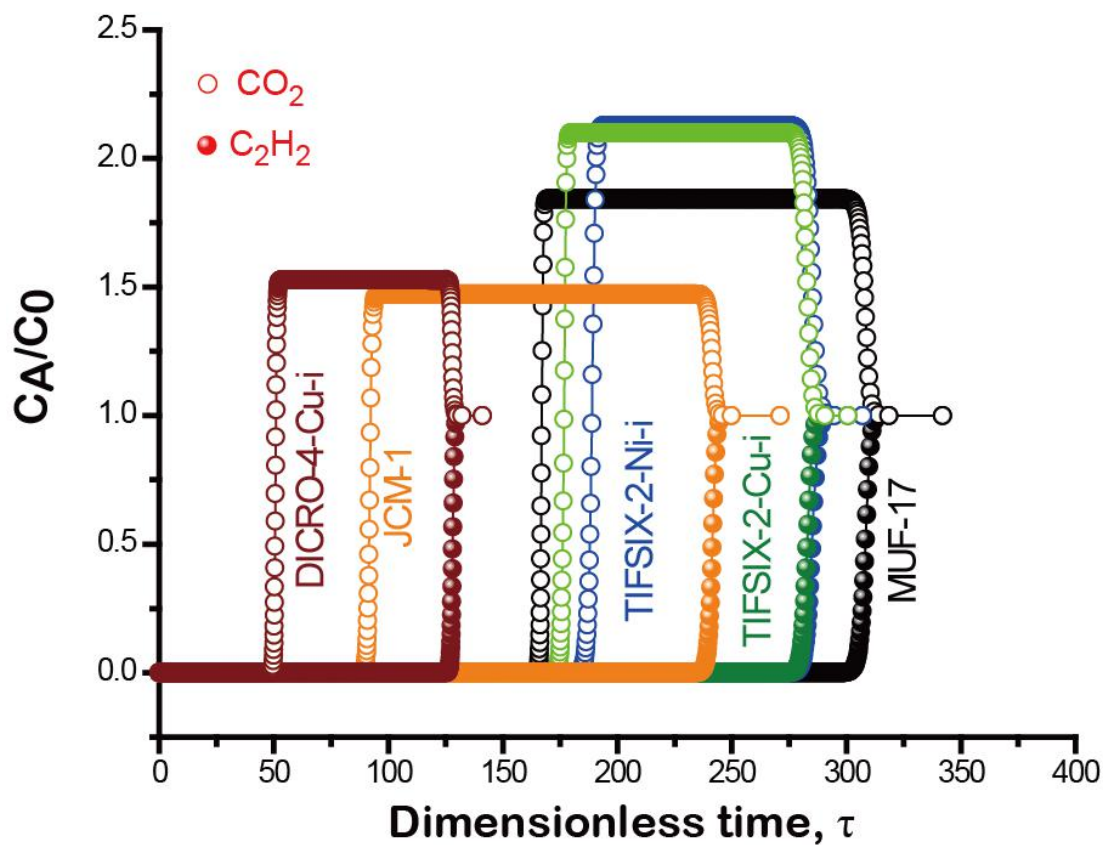


Figure S32. Simulated breakthrough curves for MUF-17, JCM-1, DICRO-4-Ni-I, TIFSIX-2-Cu-i and TIFSIX-2-Ni-i under the same conditions (length of packed bed, $L = 0.3$ m; voidage of packed bed, $\varepsilon = 0.4$; superficial gas velocity at inlet, $u = 0.04$ m/s. The x -axis is the *dimensionless* time, $\tau = t \times u / (L \times \varepsilon)$, defined by dividing the actual time, t , by the characteristic time, $L\varepsilon/u$. The materials with the same volume are used for comparison in the packed bed).

V Breakthrough Experiment Data

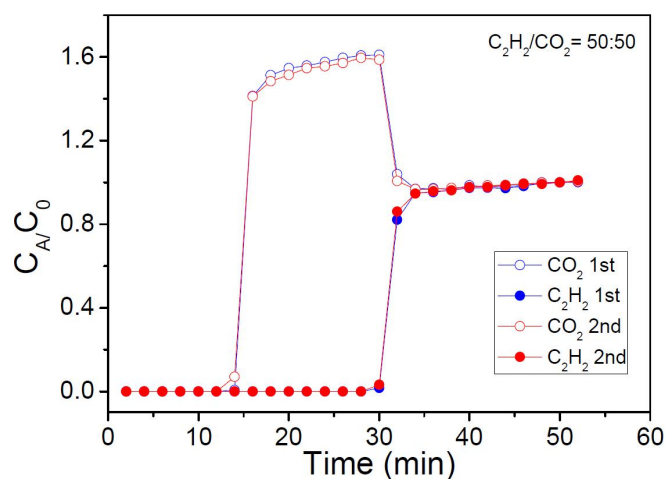


Figure S33. Repeated column breakthrough experiments (Φ 4.9 mm \times 100 mm) of C_2H_2/CO_2 (50/50) on BSF-3 (0.47 g) at ~ 2 mL/min. Curves of solid dots are about C_2H_2 , Curves of hollow dots are about CO_2 . After the first breakthrough experiment, the column was purged with a N_2 flow (5 mL min^{-1}) for 8 h at 50 $^{\circ}C$. GC monitor indicated the complete removal of C_2H_2 and CO_2 from the column.

Note: To test the breakthrough performance under high flow rate, we use a 2 fold diameter size column as the small one show distinct pressure drop during the experiments.

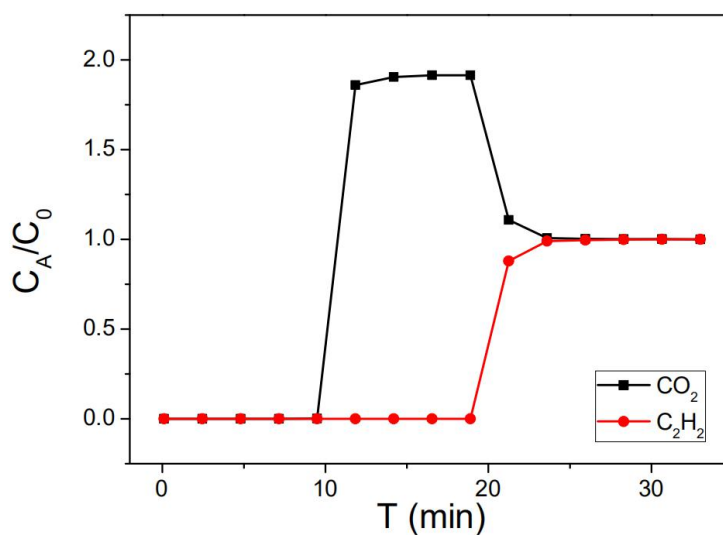


Figure S34. Column breakthrough experiments (Φ 10 mm \times 100 mm) of C_2H_2/CO_2 (50/50) on BSF-3 (1.98 g) at ~ 11 mL/min. Red Curves are about C_2H_2 . Black curves are about CO_2

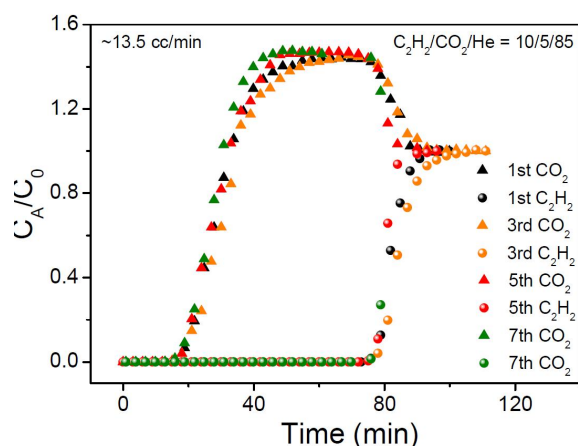


Figure S35. Repeated column breakthrough experiments (Φ 10 mm \times 100 mm) of $C_2H_2/CO_2/He$ (10/5/85) on BSF-3 (1.98 g) at \sim 13.5 mL/min. Curves of round dots are about C_2H_2 , Curves of triangular dots are about CO_2 . After every column breakthrough experiment, the column was purged with a N_2 flow (5 mL min^{-1}) for \sim 8 h at \sim 50 $^\circ\text{C}$. GC monitor indicated the complete removal of C_2H_2 and CO_2 from the column. The working capacity of acetylene was calculated to be *ca.* 2.6 mmol/g while the CO_2 adsorbed in BSF-3 was only 0.08 mmol/g, less than the static value of 0.28 mmol/g under 0.05 bar due to the competitive occupation of the binding sites by C_2H_2 . The calculated separation factor α was 16 ($\alpha = (q_1/q_2)/(y_1/y_2)$), in good agreement with the IAST selectivity (15.6) for C_2H_2/CO_2 (2:1) at 0.15 bar.

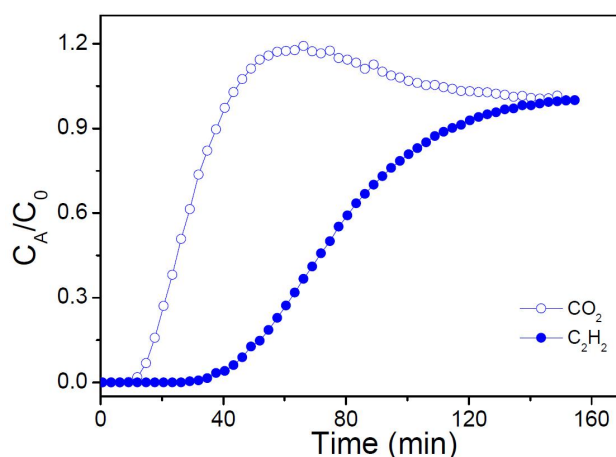


Figure S36. Column breakthrough experiments (Φ 10 mm \times 100 mm) of $C_2H_2/CO_2/He$ (10/5/85) on BSF-1 (2.13 g) at \sim 5.7 mL/min. Curves of solid dot are about C_2H_2 , Curves of hollow dot are about CO_2 . Calculated adsorption amount of C_2H_2 on BSF-1 is *ca.* 1.12 mmol/g, consistent with the static adsorption uptake of 1.01 mol/g at 0.1 bar and 298 K. Calculated adsorption amount of CO_2 is *ca.* 0.15 mmol/g. Therefore, the separation factor is \sim 3.7, in good agreement with the IAST selectivity of \sim 4.

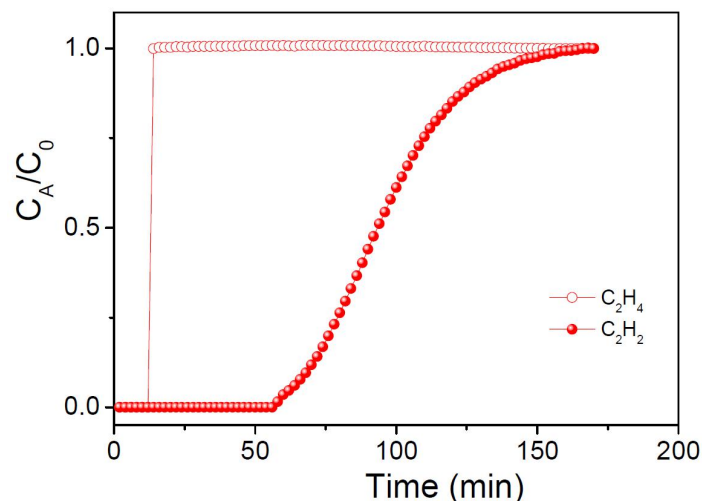


Figure S37. Column breakthrough experiments (Φ 10 mm \times 100 mm) of C_2H_2/C_2H_4 (1/99) on BSF-3 (1.98 g) at ~ 8.5 mL/min. Curves of solid dot are about C_2H_2 , Curves of hollow dot are about C_2H_4 . The processed gas mixture (within 170 min) contained 63.9 mmol of C_2H_4 and 0.645 mmol C_2H_2 . The adsorbed amount of C_2H_2 on BSF-3 was 0.354 mmol, and the adsorbed C_2H_4 amount on BSF-3 was 4.13 mmol, the separation selectivity was 8.5.

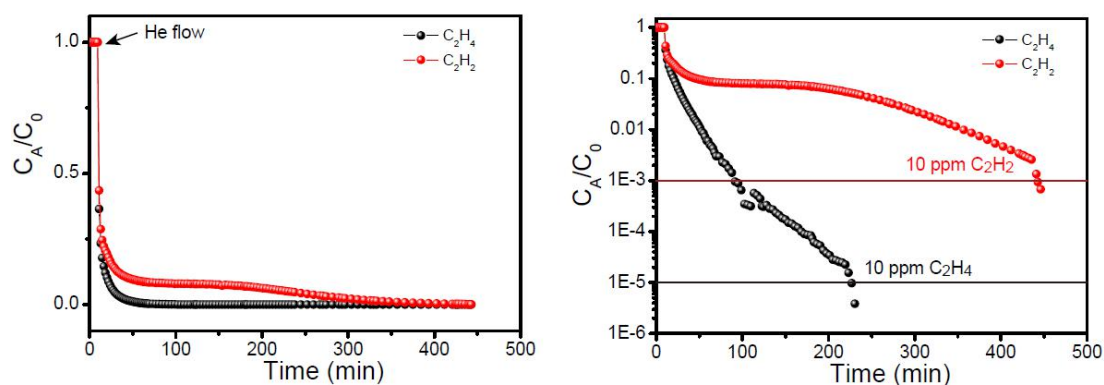


Figure S38. Regeneration test of BSF-3 by purging He flow. After column breakthrough experiments (Φ 10 mm \times 100 mm) of C_2H_2/C_2H_4 (1/99) on BSF-3 (1.98 g) at ~ 8.5 mL/min, the column was purged with a He flow (5 mL/min) at 25 $^{\circ}C$. It indicated that the outlet concentration of C_2H_4 reduced to 10 ppm after ~ 4 h while the outlet concentration of C_2H_2 reduced to 10 ppm after ~ 7 h.

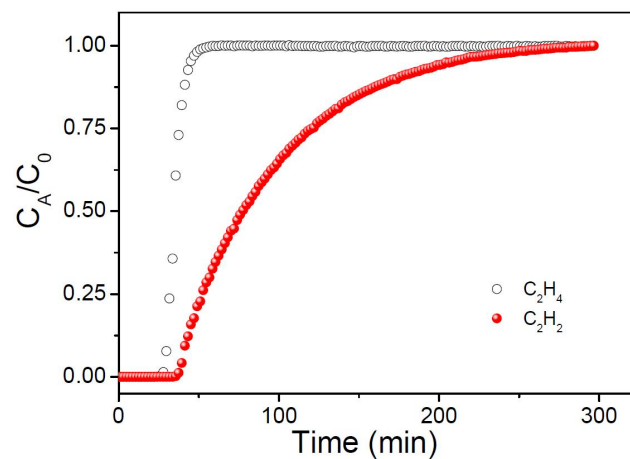


Figure S39. Column breakthrough experiments (Φ 10 mm \times 100 mm) of C_2H_2/C_2H_4 (1/99) on BSF-1 (2.13 g) at \sim 3 mL/min. Curves of solid dot are about C_2H_2 , Curves of hollow dot are about C_2H_4 .

VI. DFT calculations and GCMC simulations

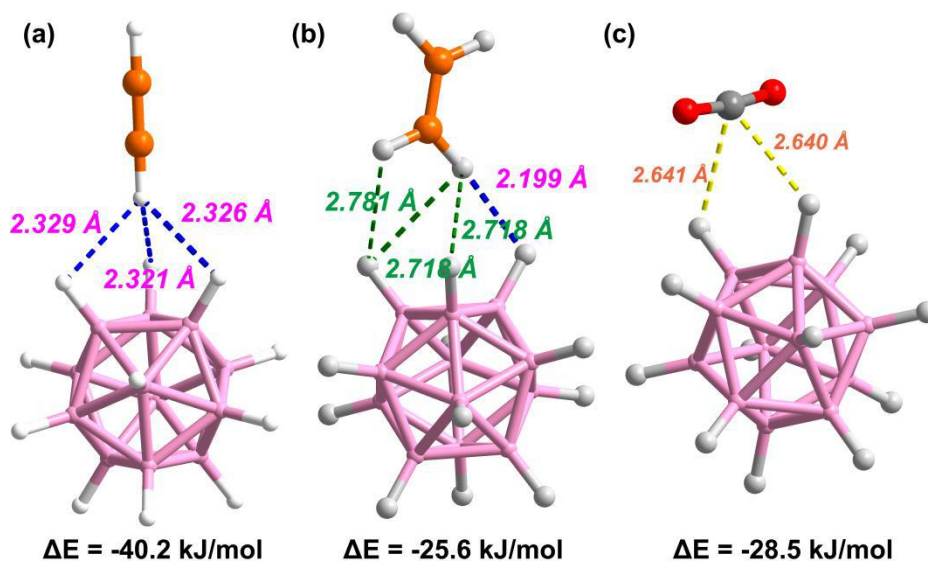


Figure S40. DFT calculated binding energy between one dodecaborate and C_2H_2 , C_2H_4 or CO_2 .

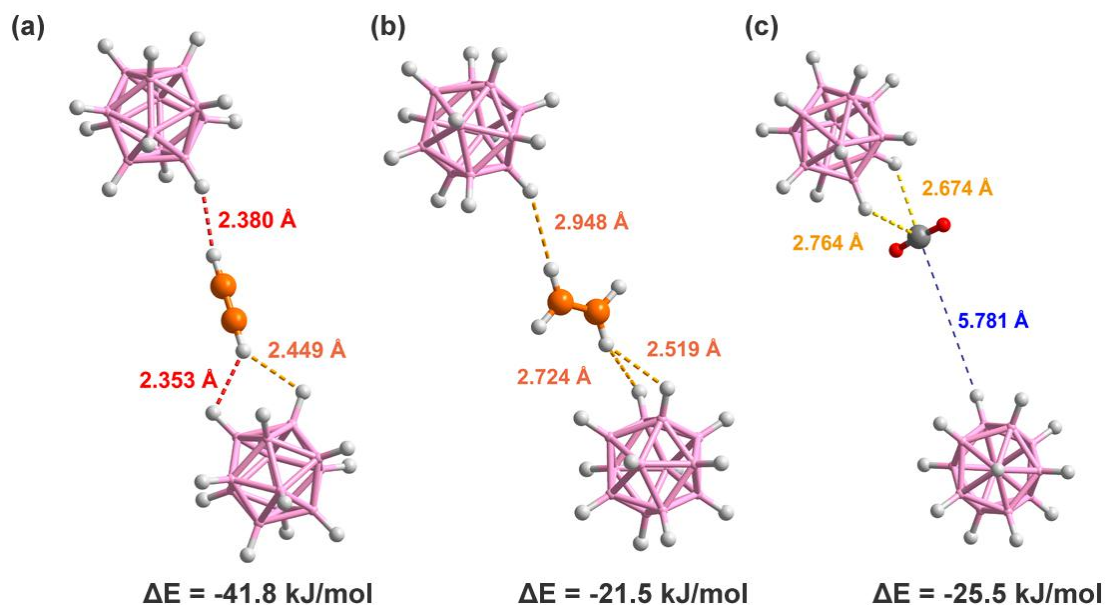


Figure S41. DFT calculated binding energy between two dodecaborates isolated from pore IIIb of BSF-3 and C_2H_2 , C_2H_4 or CO_2 .

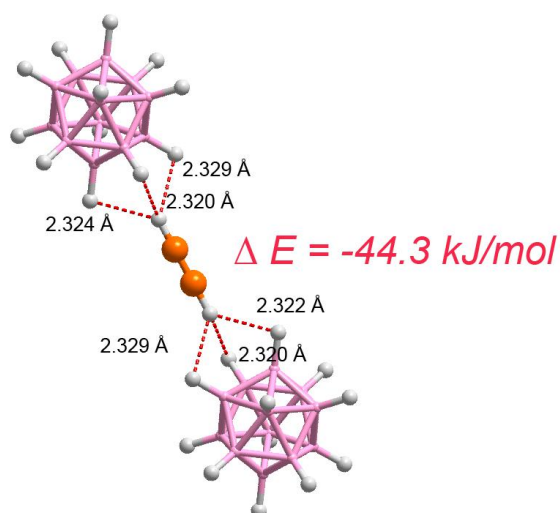


Figure S42. DFT calculated binding energy between two dodecaborates and one C₂H₂, with synergistic “3+3” dihydrogen bonds.

Interestingly, this “3+3” dihydrogen bond form is not the best form for the cooperative interactions with C₂H₂, which is probably due to the enhanced repulsion of the two dodecaborate anions under very close distance.

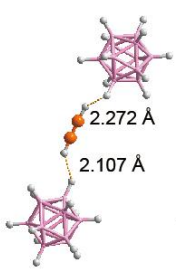
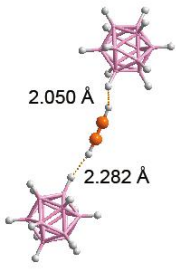
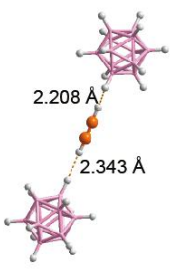
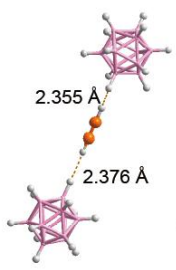
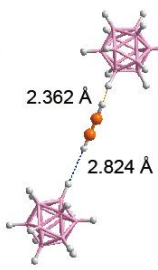
Table S11. DFT calculated binding energy between two dodecaborates and C₂H₂ by the shift of the cluster center-cluster center distance along the cluster center-cluster center connected direction

DFT optimized structure			
boron cluster center-boron cluster center distance (Å)	10	10.5	11
bonding energy (kJ/mol)	-41.98	-44.89	-47.60
DFT optimized structure			
boron cluster center-boron cluster center distance (Å)	11.5	12	12.5
bonding energy (kJ/mol)	-48.88	-47.82	-43.85

More data: with the cluster center-cluster center distance increased to 13 and 13.5 Å, the bonding energy decreased to -40.38 and -38.64 kJ/mol.

Analysis: From the bonding energy as well as the acetylene configuration between two dodecaborates, we can see that the distance between two dodecaborates is important for the interaction energy of acetylene and dodecaborates. The distance of ~11.5 Å is thought to be the optimized distance for the cooperative interactions.

Table S12. DFT calculated binding energy between two dodecaborates and C₂H₂ by the shift of the H(B)···H(B) distance along the closest H(B)···H(B) connected direction

nearest H(B)···H(B) distance (Å)	6.719	7.118	7.508	7.705	8.104
boron cluster center-boron cluster center distance (Å)	11.789	12.139	12.525	12.178	13.136
DFT optimized structure					
bonding energy (kJ/mol)	-42.61	-43.25	-41.43	-40.23	-38.48

Analysis: From the bonding energy as well as the acetylene configuration between two dodecaborates, we can see that the H(B)···H(B) distance has large effect on the interaction energy of acetylene and dodecaborate. In the range of 7.1~8.1 Å, the closer the H(B)···H(B) distance, the higher the bonding energy. Notably, in the case of 7.1 Å, the bonding energy (-43.26 kJ/mol) is already very close to the “3+3” cooperative bonding energy (-44.3 kJ/mol) from two free dodecaborate and one acetylene (Figure S58). Further decreasing the distance will lead to lower bonding energy.

From the Table S11 and Table S12, we can see that both the boron center-boron center distance and the H(B)···H(B) distance are important for the cooperative interactions. There exists the best distance that allow the strongest cooperative interactions.

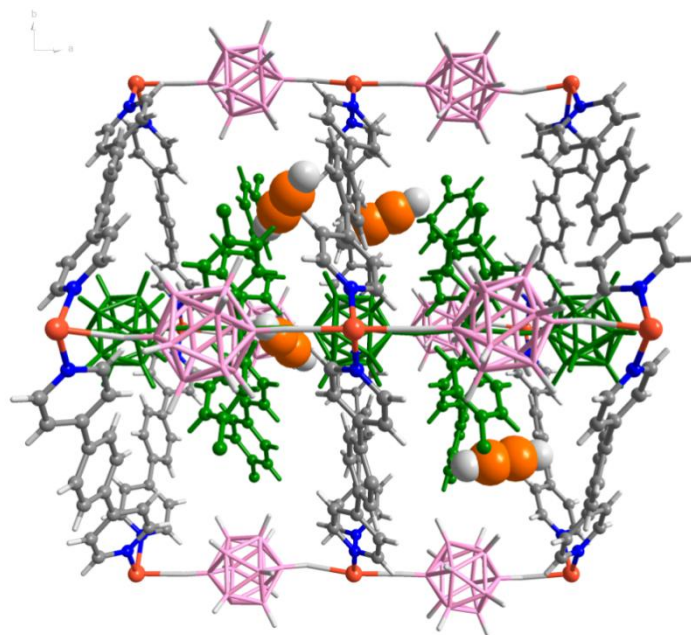


Figure S43. A snapshot from GCMC simulation results for C_2H_2 adsorption in BSF-3 along c axis at 1 kPa and 298 K. (corresponding to Figure 3a)

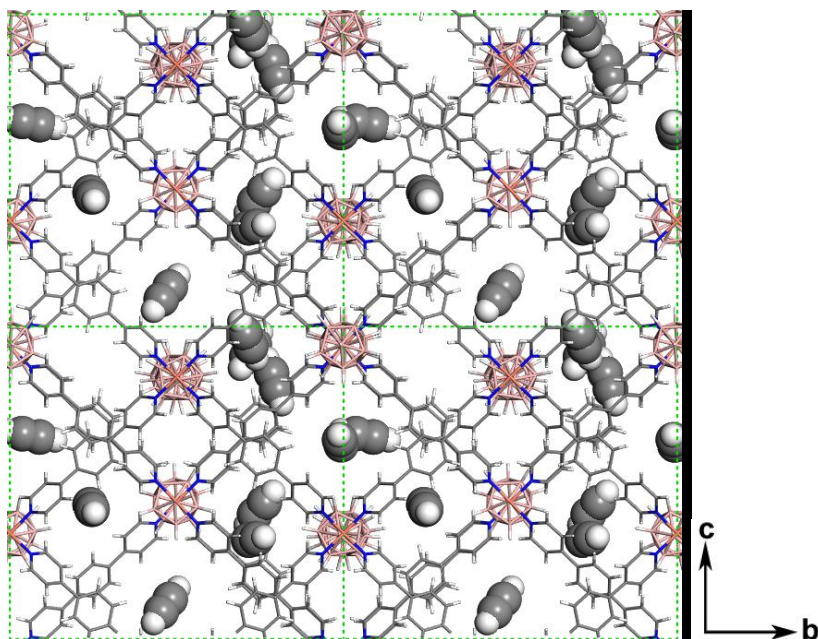


Figure S44. A snapshot from GCMC simulation results for C_2H_2 adsorption in BSF-3 ($2 \times 2 \times 2$, along a axis) at 1 kPa and 298 K. (BSF-3 is presented in stick mode and C_2H_2 (carbon, gray; hydrogen, white) is presented in space-fill mode).

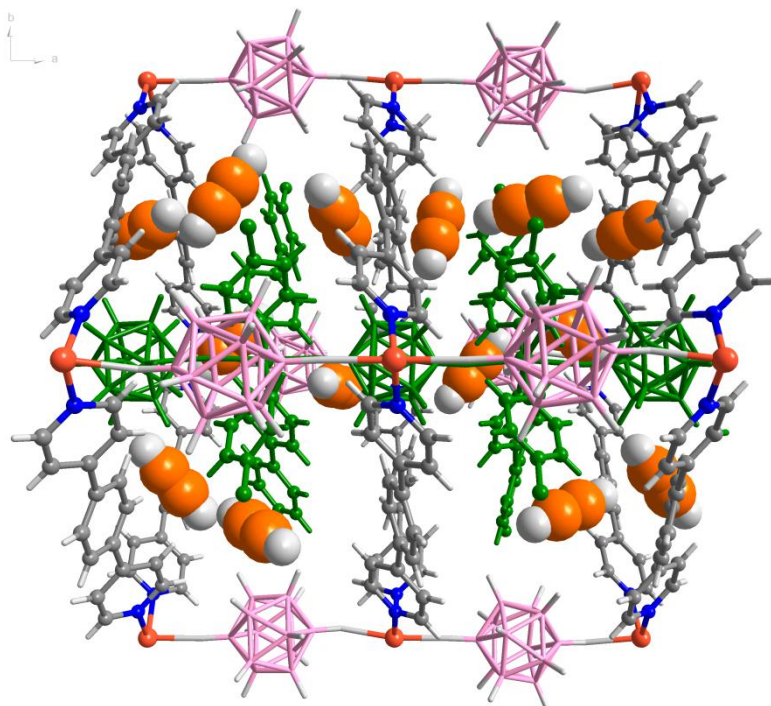


Figure S45. A snapshot from GCMC simulation results for C_2H_2 adsorption in BSF-3 along c axis at 100 kPa and 298 K. (corresponding to Figure 3b)

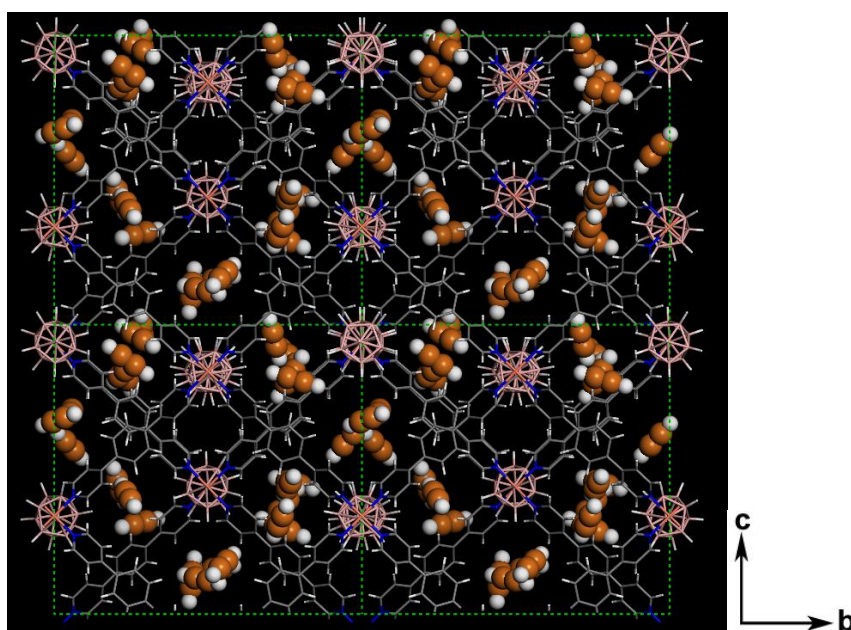


Figure S46. A snapshot from GCMC simulation results for C_2H_2 adsorption in BSF-3 ($2 \times 2 \times 2$ packing, along a axis) at 100 kPa and 298 K. (BSF-3 is presented in stick mode and C_2H_2 (carbon, orange; hydrogen, white) is presented in space-fill mode). The C_2H_2 molecules are located in the Pore I, II and III.

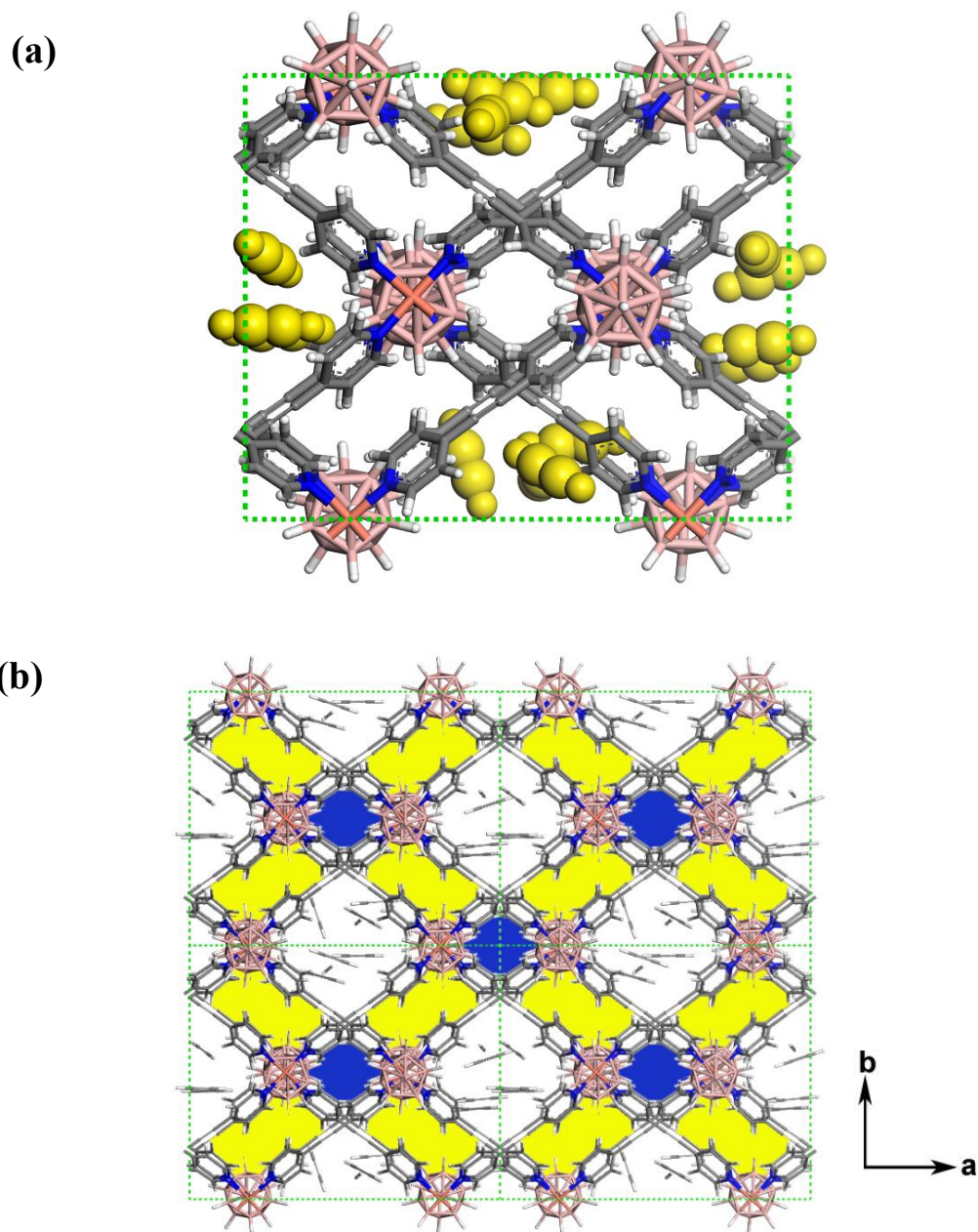


Figure S47. A snapshot from GCMC simulation results for C₂H₂ adsorption in BSF-1 at 100 kPa and 298 K along c axis. (a) in 1 × 1 × 1 packing, BSF-1 is presented in stick mode and C₂H₂ highlighted in yellow is presented in space-fill mode; (b) in 2 × 2 × 2 packing, BSF-1 and C₂H₂ (carbon, gray; hydrogen, white) are both presented in stick mode; the three inaccessible channels are highlighted by yellow or blue color.

From above GCMC simulation results, we can conclude that the C₂H₂ molecules are only adsorbed in the largest pore of BSF-1 while other pores are inaccessible.

VII. Stability Test

The stability of BSF-3 and BSF-3-Co was studied by PXRD. Leaving the activated BSF-3 in humid air for 24 h or soaking into water for 24 h did not change the PXRD pattern of BSF-3. In addition, The PXRD pattern almost kept the same after soaking into water for 40 days. When compared, BSF-3-Co was less stable towards water, putting activated BSF-3-Co into water lead to an immediate color change from yellow to pink, indicating the decomposition of BSF-3-Co and formation of a new structure (most probably be $\text{CoB}_{12}\text{H}_{12}(\text{bpb})_2(\text{H}_2\text{O})$).

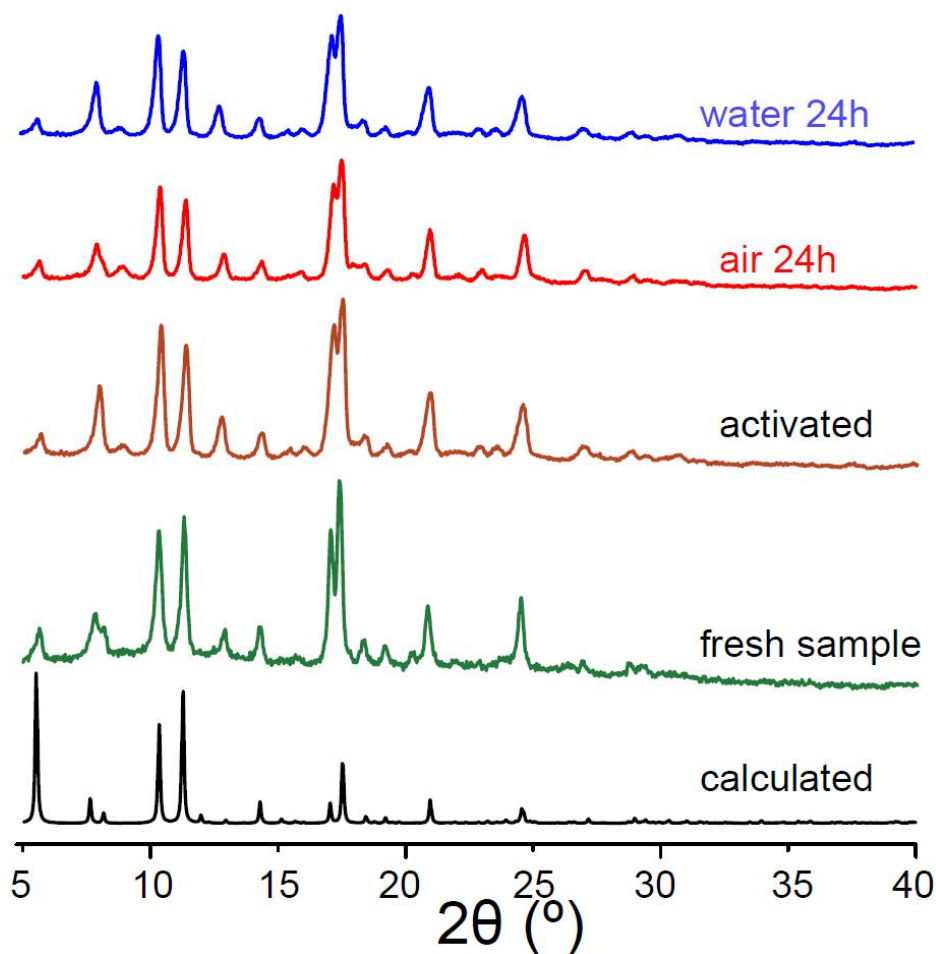


Figure S48. Powder X-ray diffraction (PXRD) patterns of BSF-3 calculated from crystal X-ray structure data (black), as-synthesized (green), activated (brown), after exposure to air for 1 day (red), treated with water for 1 day (blue). The consistent PXRD patterns indicate that BSF-3 was relatively stable towards short time exposure towards air and water.

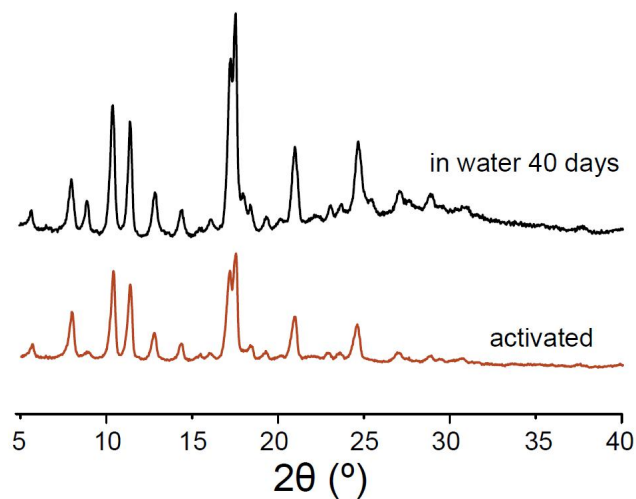


Figure S49. Powder X-ray diffraction (PXRD) patterns of BSF-3 after activation (brown), soaked in water after 40 days (black).

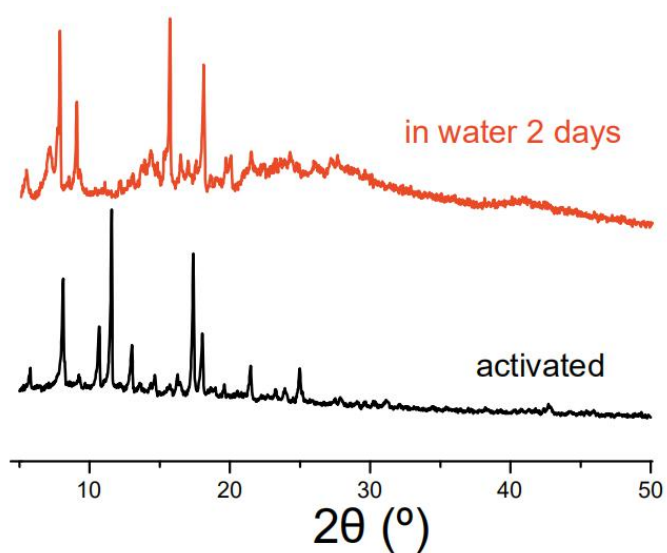


Figure S50. Powder X-ray diffraction (PXRD) patterns of BSF-3-Co after activation (black), soaked in water after 2 days (red).

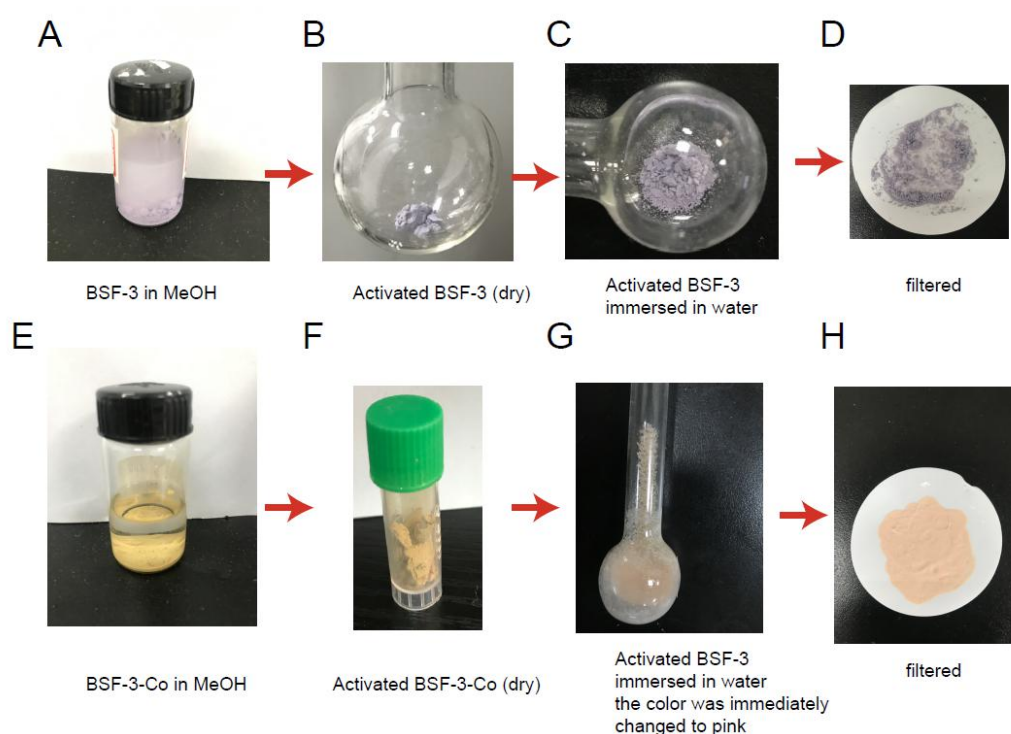


Figure S51. The color change for BSF-3 and BSF-3-Co in different states. (A) BSF-3 soaked in MeOH; (B) BSF-3 was activated at 75 °C under vacuum for 8 h; (C) activated BSF-3 immersed in water; (D) BSF-3 after filtration; (E) BSF-3-Co soaked in MeOH; (F) BSF-3-Co was activated at 75 °C under vacuum for 8 h; (G) activated BSF-3 immersed in water; (H) BSF-3-Co after filtration;

As PXRD may not reflect the tiny change of the structures, the stability of BSF-3 and BSF-3-Co were further studied by gas adsorption experiments. Leaving BSF-3 in humid air for 1 days did not influence the C_2H_2 adsorption isotherms of BSF-3, indicating its relative stability towards moisture. However, leaving activated BSF-3 in humid air for 2 months, the uptake of C_2H_2 at 298 K and 1 bar dropped to ~ 3.0 mmol/g while the PXRD patterns kept the same. Therefore, BSF-3 is still not stable towards long time exposure to moisture/water although the PXRD patterns exhibited no changes.

Leaving active BSF-3-Co in humid air for 2 months, the uptake of C_2H_2 at 298 K and 1 bar dropped from 3.85 mmol/g to 2.63 mmol/g; and the uptake of CO_2 dropped from 2.44 mmol/g to 1.68 mmol/g. The color was partially changed to pink.

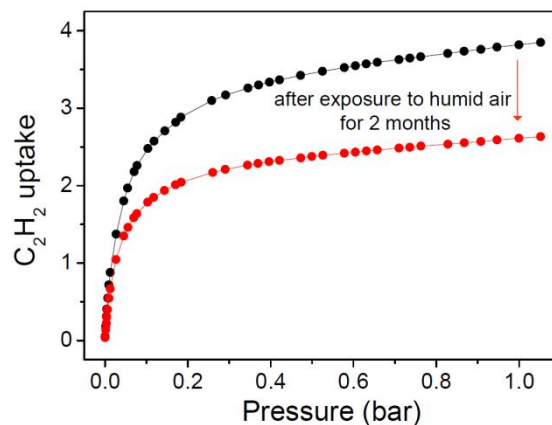


Figure S52. Adsorption isotherms of C_2H_2 on BSF-3-Co at 298 K (black, fresh activated sample; red, after exposure to air for 2 months)

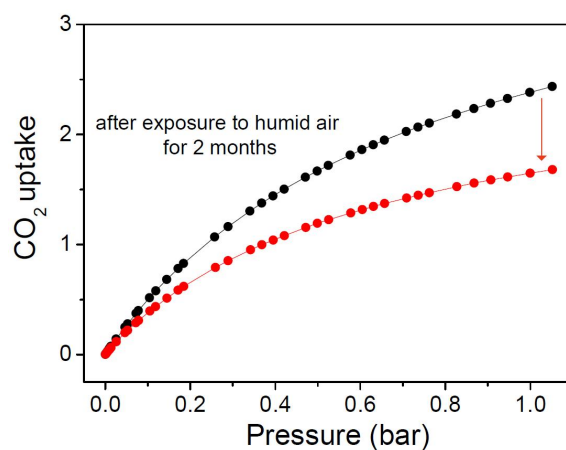


Figure S53. Adsorption isotherms of CO_2 on BSF-3-Co at 298 K (black, fresh activated sample; red, after exposure to air for 2 months)

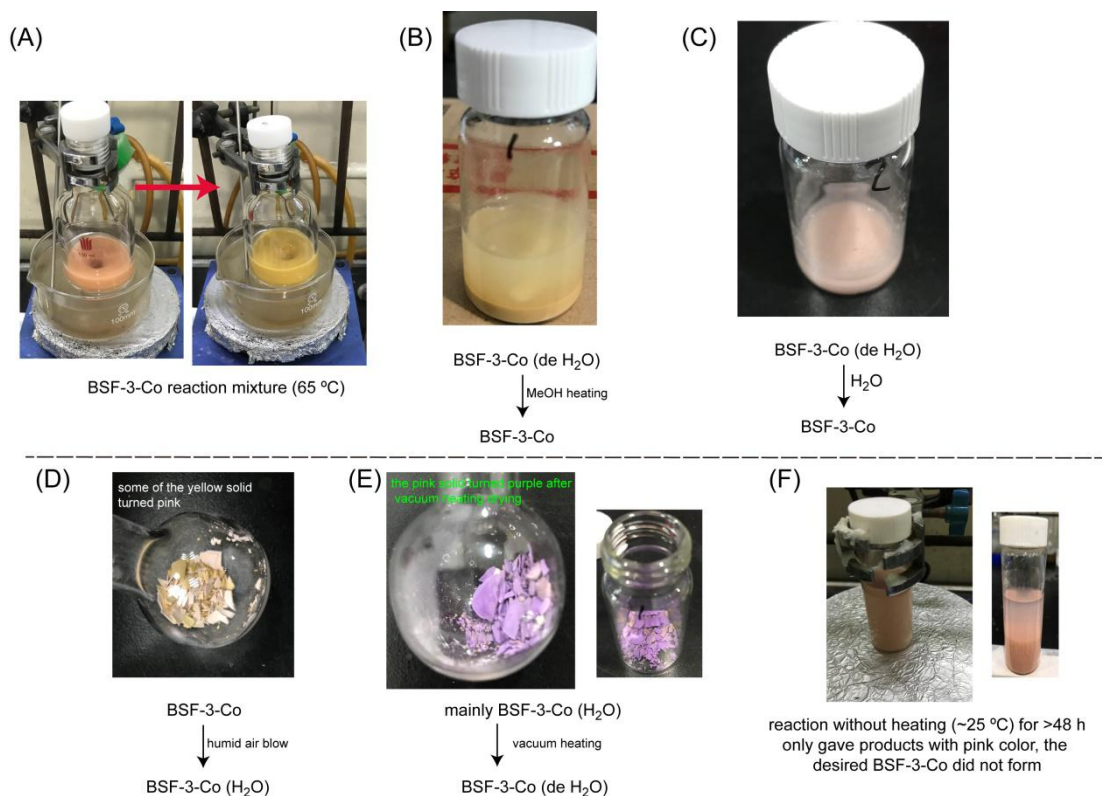


Figure S54. Photographs of color change and transformation among BSF-3-Co, BSF-3-Co (H₂O) and BSF-3-Co (de H₂O).

(A) The reaction of [Co]²⁺, [B₁₂H₁₂]²⁻ and dpb under heating temperature leads to BSF-3-Co with yellow brown color.

(B) BSF-3-Co (de H₂O) was changed to BSF-3-Co after heating in MeOH for several minutes identified by the color change (from purple to yellow brown).

(C) BSF-3-Co (de H₂O) was immediately changed to BSF-3-Co (H₂O) after addition of H₂O identified by the color change (from purple to pink).

(D) During the filtration, the BSF-3-Co on the filter paper was partially changed to BSF-3-Co (H₂O) when leaving the semi-dry powder for too long time with the wet air continually passing through.

(E) Heating the solid from Figure S49D under vacuum lead to pink color transforming to purple color with the yellow color remaining, indicating a change from BSF-3-Co (H₂O) to BSF-3-Co (de H₂O) while BSF-3-Co kept the same structure.

(F) The reaction of [Co]²⁺, [B₁₂H₁₂]²⁻ and dpb under 25 °C *cannot* lead to BSF-3-Co, indicating the removal of coordinated H₂O on the Co(II) needs more energy than the removal of coordinated H₂O on the Cu(II) (BSF-3 can also be prepared under room temperature. The product showed the same PXRD patterns but slightly lower gas uptake).

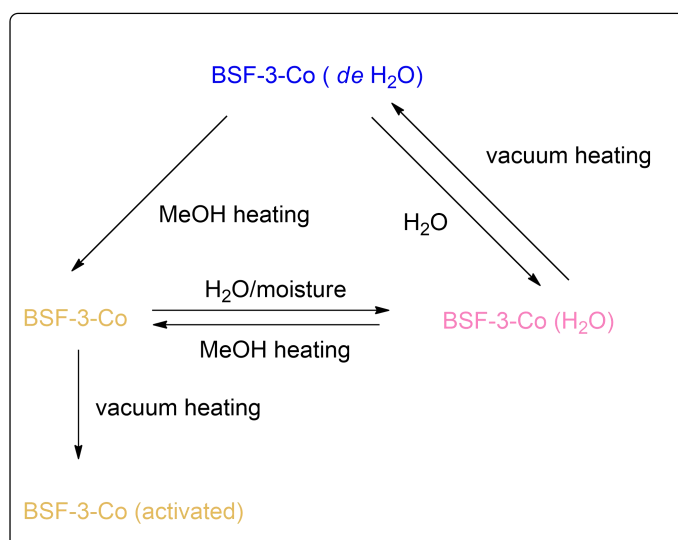
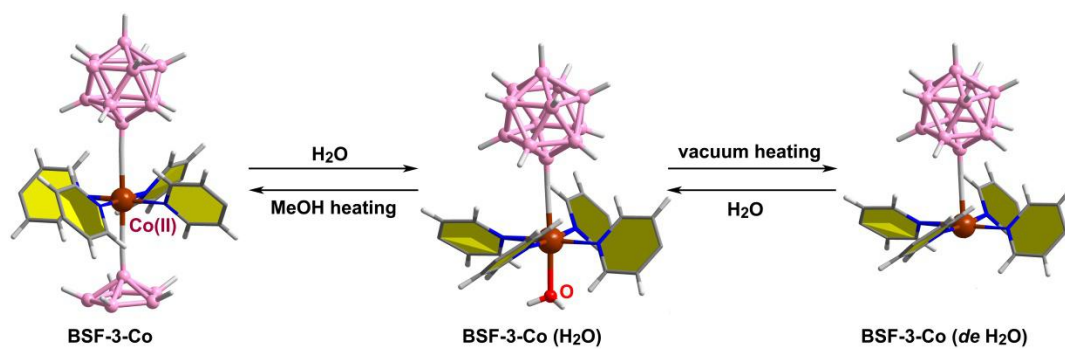


Figure S55. Proposed structure change among BSF-3-Co, BSF-3-Co (H₂O) and BSF-3-Co (*de* H₂O)

VIII Adsorption selectivity comparison table

Material Name	C ₂ H ₂ (mL/g)	CO ₂ (mL/g)	C ₂ H ₄ (mL/g)	V _{C₂H₂} / V _{CO₂}	V _{C₂H₂} / V _{C₂H₄}	S _{C₂H₂/CO₂} or/and S _{C₂H₂/C₂H₄}	Ref.
HKUST-1	201	113	-	1.78	-		[3]
MAF-2	70	19	-	3.68	-		[4]
MFM-188 ^[b]	232.6	120.7	-	1.93	-		[5]
Mg(HCOO) ₂	66	45	-	1.47	-		[6]
Mg-MOF-74	184.4	179.2	-	1.03	-		[7]
UTSA-74 ^[c]	108.2	70.9	-	1.53	-	9.0	[8]
ZJU-8	194.7	103.9	-	1.87	-		[9]
ZJU-40	216.2	87.6	-	2.47	-		[10]
M'-MOF-3a ^[c]	42.6		9.0		4.73		[11]
UTSA-100a ^[c]	95.6	-	37.2		2.57		[12]
NOTT-300 ^[d]	142		95.9		1.48		[13]
MOF-74-Co	183		157		1.16		[14]
JCM-1	76.5	38.1	35.7	2.01	2.14	13.7/13.2	[15]
JXNU-5	56	34.7		1.61		~6	[16]
Zn-MOF-74	108	105.5		1.02		~2.0	[8]
Zn ₂ (ATBC)	179	104				6	[17]
FJU-22a ^[c]	114.8	111.3	85.8	1.03	1.34		[18]
NKMOF-1-Ni	61.0	51.1	47.3	1.19	1.29	~25	[19]
HOF-3a	47.0	20.8		2.25		~22	[20]
DICRO-4-Ni-i	43.0	23.1		1.87		13.9	[21]
TIFSIX-2-Cu-i	91.8	96.3		0.95		6.5 ^[e]	[22]
[Ni ₃ (HCOO) ₆]	53.4	37.0		1.44		22	[23]
TIFSIX-2-Ni-i	94.3	101.7		0.95		6.1	[24]
PCP-33	121.8	58.6	86.8	2.08	1.40	~6/~2	[25]
SIFSIX-1-Cu	190.4	107.9	92.1	1.74	2.07		[26]
SIFSIX-2-Cu-i	90.0	108.4	49.1	0.83	1.84		[26]
SIFSIX-3-Zn	81.5	57.0	50.2	1.43	1.62		[26]
UTSA-300a	68.9	3.25	0.92	21.2	74.9		[27]
MUF-17 ^d	61.3	51.1	43.8	1.20	1.40	6.01/8.76	[28]
FJU-90a	180	103		1.75		4.3	[29]
[Cu(BDC-Br) (H ₂ O _{0.5} DMF) _{2.5}]	34.3	24.2		1.42		4	[30]
SNNU-45	134	97.4		1.38		4.5	[31]
JNU-1	60	48		1.25		< 5	[32]
BSF-1	52.6	39.6	36.5	1.20	1.44	3.4/2.4	This work
BSF-2	41.4	29.8	29.6	1.39	1.40	5.1/2.9	
BSF-3	81.8	47.3	53.1	1.73	1.54	16.3/8.0	
BSF-3-Co	86.2	51.7	56.2	1.60	1.53	12.7/10.2	

[a] all conditions are under 298 K and 1 bar, equimolar selectivity unless stated; [b] C₂H₂: 295 K, CO₂: 298 K; [c] 296 K; [d] 293 K; [e] C₂H₂/CO₂ = 2:1.

Table S13. Summary of adsorption and selectivities/ratio in various MOFs. ^[a]

References

- [1] (a) V. Geis, K. Guttische, C. Knapp, H. Scherer, R. Uzun, *Dalton Trans.* **2009**, 2687–2694; (b) W. H. Knoth, H. C. Miller, J. C. Sauer, J. H. Balthis, Y. T. Chia, E. L. Muetterties, *Inorg Chem.* **1964**, *3*, 159–167; (c) T. Peymann, C. B. Knobler, M. F. Hawthorne, *Inorg. Chem.* **2000**, *39*, 1163–1170.
- [2] (a) R. Krishna, *RSC Adv.* **2017**, *7*, 35724–35737; (b) R. Krishna, *Sep. Purif. Technol.* **2018**, *194*, 281–300; (c) R. Krishna, *Microporous Mesoporous Mater.* **2014**, *185*, 30–50; (d) R. Krishna, *RSC Adv.* **2015**, *5*, 52269–52295.
- [3] M. Fischer, F. Hoffmann, M. Froba, *Chemphyschem* **2010**, *11*, 2220–2229.
- [4] J. P. Zhang, X. M. Chen, *J. Am. Chem. Soc.* **2009**, *131*, 5516–5521.
- [5] F. Moreau, I. da Silva, N. H. Al Smail, T. L. Easun, M. Savage, H. G. W. Godfrey, S. F. Parker, P. Manuel, S. H. Yang, M. Schroder, *Nat Commun* **2017**, *8*, 14085
- [6] D. G. Samsonenko, H. Kim, Y. Sun, G. H. Kim, H. S. Lee, K. Kim, *Chem Asian J* **2007**, *2*, 484–488.
- [7] (a) S. R. Caskey, A. G. Wong-Foy, A. J. Matzger, *J. Am. Chem. Soc.* **2008**, *130*, 10870–10871; (b) S. Xiang, W. Zhou, Z. Zhang, M. A. Green, Y. Liu, B. Chen, *Angew. Chem. Int. Ed. Engl.* **2010**, *49*, 4615–4618.
- [8] F. Luo, C. Yan, L. Dang, R. Krishna, W. Zhou, H. Wu, X. Dong, Y. Han, T. L. Hu, M. O’Keeffe, L. Wang, M. Luo, R. B. Lin, B. Chen, *J. Am. Chem. Soc.* **2016**, *138*, 5678–5684.
- [9] J. Cai, H. Wang, H. Wang, X. Duan, Z. Wang, Y. Cui, Y. Yang, B. Chen, G. Qian, *RSC Adv.* **2015**, *5*, 77417–77422.
- [10] H. M. Wen, H. Wang, B. Li, Y. Cui, H. Wang, G. Qian, B. Chen, *Inorg. Chem.* **2016**, *55*, 7214–7218.
- [11] S. C. Xiang, Z. Zhang, C. G. Zhao, K. Hong, X. Zhao, D. R. Ding, M. H. Xie, C. D. Wu, M. C. Das, R. Gill, K. M. Thomas, B. Chen, *Nat Commun* **2011**, *2*, 204.
- [12] T. L. Hu, H. Wang, B. Li, R. Krishna, H. Wu, W. Zhou, Y. Zhao, Y. Han, X. Wang, W. Zhu, Z. Yao, S. Xiang, B. Chen, *Nat. Commun* **2015**, *6*, 7328.
- [13] S. Yang, A. J. Ramirez-Cuesta, R. Newby, V. Garcia-Sakai, P. Manuel, S. K. Callear, S. I. Campbell, C. C. Tang, M. Schroder, *Nat Chem* **2014**, *7*, 121–129.
- [14] Y. He, R. Krishna, B. Chen, *Energy & Environmental Science* **2012**, *5*, 9107.

- [15] J. Lee, C. Y. Chuah, J. Kim, Y. Kim, N. Ko, Y. Seo, K. Kim, T. H. Bae, E. Lee, *Angew. Chem. Int. Ed.* **2018**, *57*, 7869–7873.
- [16] R. Liu, Q.-Y. Liu, R. Krishna, W. Wang, C.-T. He, Y.-L. Wang, *Inorg. Chem.* **2019**, *58*, 5089–5095.
- [17] C.-L. Gao, *Inorg. Chem. Commun.* **2019**, *105*, 4–8
- [18] Z. Z. Yao, Z. J. Zhang, L. Z. Liu, Z. Y. Li, W. Zhou, Y. F. Zhao, Han, Y. B. L. Chen, R. Krishna, S. C. Xiang, *Chem. - Eur. J.* **2016**, *22*, 5676–5683.
- [19] Y.-L. Peng, T. Pham, P. Li, T. Wang, Y. Chen, K.-J. Chen, K. A. Forrest, B. Space, P. Chen, M. J. Zaworotko, Z. Zhang, *Angew. Chem. Int. Ed.* **2018**, *57*, 10971–10975
- [20] P. Li, Y. He, Y. Zhao, L. Weng, H. Wang, R. Krishna, H. Wu, W. Zhou, M. O’Keeffe, Y. Han, B. Chen, *Angew. Chem. Int. Ed.* **2015**, *54*, 574–577.
- [21] H. S. Scott, M. Shivanna, A. Bajpai, D. G. Madden, K.-J. Chen, T. Pham, K. A. Forrest, A. Hogan, B. Space, J. J. Perry IV., M. J. Zaworotko, *ACS Appl. Mater. Interfaces*, **2017**, *9*, 33395–33400
- [22] K.-J. Chen, H. S. Scott, D. G. Madden, T. Pham, A. Kumar, A. Bajpai, M. Lusi, K. A. Forrest, B. Space, J. J. Perry IV, M. J. Zaworotko, *Chem*, **2016**, *1*, 753–765.
- [23] L. Zhang, K. Jiang, J. Zhang, J. Pei, K. Shao, Y. Cui, B. Li, B. Chen, G. Qian, *ACS Sustainable Chem. Eng.* **2019**, *71*, 1667–1672
- [24] M. Jiang, X. Cui, L. Yang, Q. Yang, Z. Zhang, Y. Yang, H. Xing, *Chem. Eng. J.* **2018**, *352*, 803–810.
- [25] J. Duan, W. Jin, R. Krishna, *Inorg. Chem.* **2015**, *54*, 4279–4284.
- [26] X. Cui, K. Chen, H. Xing, Q. Yang, R. Krishna, Z. Bao, H. Wu, W. Zhou, X. Dong, Y. Han, B. Li, Q. Ren, M. J. Zaworotko, B. Chen, *Science* **2016**, *353*, 141–144.
- [27] R. B. Lin, L. Li, H. Wu, H. Arman, B. Li, R. G. Lin, W. Zhou, B. Chen, *J. Am. Chem. Soc.* **2017**, *139*, 8022–8028.
- [28] O. T. Qazvini; R. Babarao; S. G. Telfer; *Chem. Mater.* **2019**, *31*, 4919–4926.
- [29] Y. Ye, Z. Ma, R. Krishna, W. Zhou, Q. Lin, Z. Zhang, S. Xiang, B. Chen, *J. Am. Chem. Soc.* **2019**, *141*, 4130–4136.
- [30] H. Cui, Y. Ye, H. Arman, Z. Li, A. Alsame, R.-B. Lin, B. Chen, *Cryst. Growth Des.* **2019**, DOI: 10.1021/acs.cgd.9b00850.
- [31] Y.-P. Li, Y. Wang, Y. Y. Xue, H.-P. Li, Q.-G. Zhai, S.-N. Li, Y. -C. Jiang, M.-C. Hu, X. Bu, *Angew. Chem. Int. Ed.* **2019**, *58*, 13590–13595.

- [32] H. Zeng, M. Xie, Y.-L. Huang, Y. Zhao, X.-J. Xie, J. P. Bai, M. Y. wan, R. Krishna, W. Lu, D. Li, *Angew. Chem. Int. Ed.* **2019**, *58*, 8515–8519.
- [33] Y. B. Zhang, L. F. Yang, L. Y. Wang, S. Duttwyler, H. B. Xing, *Angew. Chem. Int. Ed.*, **2019**, *58*, 8145–8150